Apodization of chirped quasi-phasematching devices

C. R. Phillips,[1,2,*] C. Langrock,[1] D. Chang,[1] Y. W. Lin,[1] L. Gallmann,[2] and M. M. Fejer[1]

[1]*Edward L. Ginzton Laboratory, Stanford University, Stanford, California 94305, USA*
[2]*Department of Physics, Institute of Quantum Electronics, ETH Zurich, Zurich 8093, Switzerland*
**Corresponding author: cphillips@phys.ethz.ch*

Received February 25, 2013; accepted March 28, 2013;
posted April 17, 2013 (Doc. ID 185964); published May 15, 2013

Chirped quasi-phasematching (QPM) optical devices offer the potential for ultrawide bandwidths, high conversion efficiencies, and high amplification factors across the transparency range of QPM media. In order to properly take advantage of these devices, apodization schemes are required. We study apodization in detail for many regimes of interest, including low-gain difference frequency generation (DFG), high-gain optical parametric amplification (OPA), and high-efficiency adiabatic frequency conversion (AFC). Our analysis is also applicable to second-harmonic generation, sum frequency generation, and optical rectification. In each case, a systematic and optimized approach to grating construction is provided, and different apodization techniques are compared where appropriate. We find that nonlinear chirp apodization, where the poling period is varied smoothly, monotonically, and rapidly at the edges of the device, offers the best performance. We consider the full spatial structure of the QPM gratings in our simulations, but utilize the first order QPM approximation to obtain analytical and semi-analytical results. One application of our results is optical parametric chirped pulse amplification; we show that special care must be taken in this case to obtain high gain factors while maintaining a flat gain spectrum.

OCIS codes: (190.4360) Nonlinear optics, devices; (230.7405) Wavelength conversion devices; (190.4970) Parametric oscillators and amplifiers; (320.7080) Ultrafast devices.
http://dx.doi.org/10.1364/JOSAB.30.001551

1. INTRODUCTION

Chirped (aperiodic) quasi-phasematching (QPM) gratings have received attention for various optical frequency conversion schemes, including difference frequency generation (DFG), optical parametric amplification (OPA), sum frequency generation (SFG), optical parametric oscillators (OPOs), and many other applications [1–23]. Their main role so far has been to broaden the phasematching bandwidth compared to conventional periodic QPM gratings, without the need to use short crystals with reduced conversion efficiency, tighter focusing, or higher intensities. This broadening can be understood through a simple spatial frequency argument: due to dispersion, there is a mapping between phasematched frequency and grating k-vector; in chirped QPM gratings, the grating k-vector is swept smoothly over the range of interest, thereby broadening the spatial Fourier spectrum of the grating and hence the phasematching bandwidth.

For continuous wave (cw) interactions involving the generation of a weak wave from two undepleted waves, the generation of the output wave can be described in terms of the spatial Fourier transform of the QPM grating evaluated at the spatial frequency corresponding to the phase mismatch associated with the three-wave interaction [2]. This type of interaction corresponds, for example, to negligible pump depletion and low signal amplification in OPA, or to second-harmonic generation (SHG) with negligible pump depletion. Since the nonlinear polarization is abruptly turned on at the edges of the nonlinear crystal, this QPM transfer function exhibits an interference effect associated with the corresponding high spatial frequency components. Such a spectral ripple is highly undesirable in most applications.

In order to remove the spectral ripple, apodization techniques may be employed to bring some measure of the effective nonlinearity smoothly to zero [1,24–27]. Several schemes have been proposed, including deleted domains, duty cycle variation, waveguide tapering [24], the use of nonlinear chirp profiles [1], and step-chirp designs [26].

In the context of apodization, we take linearity to mean that the output wave of interest is linear in the nonlinear coefficient $d(z)$. In many cases of practical interest, the assumption of linearity does not hold. For example, in high-gain OPA employing chirped QPM gratings, apodization is particularly important [1]. Furthermore, relatively recently it has been shown that saturated nonlinear interactions in chirped QPM gratings can exhibit high efficiencies due to an adiabatic following process [7,8]. As a result of this process, for three-wave mixing (TWM) processes involving input pump and signal waves and a generated idler wave, the ratio of pump output and input intensities approaches 0 with respect to both the input signal and pump intensities, i.e., approaches 100% pump depletion. This behavior, termed adiabatic frequency conversion (AFC), occurs for interactions that are both plane wave and monochromatic, provided that the QPM grating is sufficiently chirped.

In this paper, we study apodization for various different types of operating regimes of interest to chirped QPM devices, including low-gain and low-efficiency interactions such as DFG, high-gain OPA interactions, and even AFC. We show how apodization profiles can be constructed systematically, and how their construction can be connected with the underlying structure of the TWM process in an intuitive way. This approach enables high performance, limited only by the

inherently discrete QPM grating structure. We analyze all of the designs presented in detail numerically, in particular taking into account the full nonlinear evolution of the coupled waves in the actual discrete QPM structure (as opposed to assuming a simplified first order QPM interaction). Our study will enable the continued development of many different chirped QPM devices and technologies.

In Section 2, we establish the CWEs that will be used in the remaining sections. In Section 3, we solve these equations for the simple case of DFG in a chirped QPM grating, highlighting the connection between these solutions and the eigenmodes of the relevant CWE. In Section 4, we determine and compare apodization profiles for the linear cases [corresponding to DFG, SFG, SHG, optical rectification (OR), etc.]. In Section 5, we consider the case of high-gain OPA in chirped QPM devices, and establish and compare apodization techniques. In Section 6, we introduce AFC, and show in detail how these interactions can be analyzed and understood using the geometrical analysis of TWM processes developed in [28]. In Section 7, we develop apodization procedures for AFC via this geometrical analysis. We give an example apodization profile designed for the case of a moderate-gain, high-pump-depletion OPA device. Our results show that for all of the above types of interactions, and particularly for OPA and AFC, nonlinear chirp apodization offers significant advantages over other approaches, such as deleted domain apodization (DDA). Last, we conclude and discuss several important practical aspects of our results in Section 8.

2. COUPLED WAVE EQUATIONS

In this section, we introduce the equations governing arbitrary TWM processes in QPM devices. We consider plane wave, quasi-cw interactions, for which each signal frequency mixes with a single pump and idler frequency. Even for non-cw interactions, this assumption is very useful for studying TWM processes, for example, in optical parametric chirped pulse amplification (OPCPA) systems.

A. Three-Wave Mixing

In the quasi-cw approximation, the evolution of the electric field in the QPM grating is given by the coupled wave equations (CWEs) [29]:

$$\frac{dA_i}{dz} = -i\frac{\omega_i d_0}{n_i c}\bar{d}(z)A_s^* A_p e^{-i\Delta k_0 z}, \tag{1a}$$

$$\frac{dA_s}{dz} = -i\frac{\omega_s d_0}{n_s c}\bar{d}(z)A_i^* A_p e^{-i\Delta k_0 z}, \tag{1b}$$

$$\frac{dA_p}{dz} = -i\frac{\omega_p d_0}{n_p c}\bar{d}(z)A_i A_s e^{+i\Delta k_0 z}, \tag{1c}$$

where subscripts i, s, and p denote quantities associated with the idler, signal, and pump envelopes, respectively. The normalized nonlinear coefficient $\bar{d}(z)$ is defined in terms of the spatially varying nonlinear coefficient $d(z)$ as $\bar{d}(z) = d(z)/d_0$, where d_0 is the nonlinear coefficient in the unmodulated material. ω_j is the angular optical frequency of wave j (these satisfy $\omega_p = \omega_i + \omega_s$), and n_j is refractive index of wave j. The material phase mismatch Δk_0 is given by $\Delta k_0 = k_p - k_s - k_i$, where $k_j = \omega_j n_j/c$ is the wavevector for wave j. The electric field envelopes A_j are assumed here for simplicity to contain only a single frequency component, and are defined such that the total electric field is given by

$$E(z,t) = \frac{1}{2}\sum_j A_j(z)\exp[i(\omega_j t - k_j z)] + \text{c.c.}, \tag{2}$$

where c.c. denotes complex conjugate.

Note that when pulsed interactions are analyzed within the quasi-cw limit, a set of CWEs similar to Eqs. (1) should be found, and expressed in the frequency domain, since the coupling coefficients $(\omega_j d_0)/(n_j c)$ and phase mismatch Δk are frequency dependent.

B. Quasi-Phasematching

Equations (1) apply for arbitrary spatial profiles of the nonlinear coefficient $d(z)$, provided that backward waves can be neglected. In a QPM grating, $d = \pm d_0$. Because of this constraint, it is possible to write arbitrary QPM grating profiles in a Fourier series:

$$\bar{d}(z) \equiv \frac{d(z)}{d_0} = \text{sgn}[\cos(\phi_G(z)) - \cos(\pi D(z))] \tag{3a}$$

$$= (2D(z) - 1) + \sum_{\substack{m=-\infty \\ m\neq 0}}^{\infty} \frac{2\sin(\pi m D(z))}{\pi m}\exp(im\phi_G(z)), \tag{3b}$$

where $D(z)$ and $\phi_G(z)$ are the grating duty cycle and phase functions, respectively. Often, $D(z) \approx 0.5$ by design, due to QPM fabrication limitations [30], minimization of photorefractive effects [31–33], and also in order to maximize the amplitude of the first Fourier order ($m = \pm 1$) in Eq. (3), but we consider more general cases here. In chirped QPM gratings, the phase function can be expressed as

$$\phi_G(z) = \phi_G(z_i) + \int_{z_i}^{z} K_g(z')\mathrm{d}z', \tag{4}$$

where $K_g(z)$ is the smooth and continuous local grating k-vector (or local spatial frequency), and $\phi_G(z_i)$ is a chosen initial phase. z_i and z_f denote the positions of the input and output ends of the grating. Note that we do not assume $z_i = 0$, and therefore the $\exp(-ik_j z)$ phase factors in Eq. (2) must be accounted for in determining the *input* envelopes $A_j(z_i)$ given a known input electric field $E(z_i, t)$.

In an interaction where only one Fourier order of the QPM grating is close to the phasematching condition, $\bar{d}(z)$ can be approximated by considering only the $\pm m$th terms in Eq. (3b). In particular, for a first order QPM interaction, Eqs. (1) become

$$\frac{dA_i}{dz} = -i\kappa_i(z)A_s^* A_p e^{-i\phi_1(z)}, \tag{5a}$$

$$\frac{dA_s}{dz} = -i\kappa_s(z)A_i^* A_p e^{-i\phi_1(z)}, \tag{5b}$$

$$\frac{dA_p}{dz} = -i\kappa_p(z)A_iA_se^{+i\phi_1(z)}. \tag{5c}$$

In these equations, the coupling coefficients $\kappa_j(z)$ are given by

$$\kappa_j(z) = \frac{\omega_j d_0}{n_j c}\frac{2}{\pi}\sin(\pi D(z)), \tag{6}$$

and the accumulated phase mismatch $\phi_1(z)$ is given by

$$\phi_1(z) = \phi_1(z_i) + \int_{z_i}^{z}\Delta k_1(z')\mathrm{d}z', \tag{7}$$

where the local phase mismatch is given by

$$\Delta k_m(z) = k_p - k_s - k_i - mK_g(z), \tag{8}$$

for integer m (the QPM order), and $\phi_1(z_i)$ corresponds to the relative phase between the three envelopes and their driving terms at the input of the device. Usually, one of the envelopes is initially zero, and in such cases $\phi_1(z_i)$ has no effect on the dynamics. The first order QPM approximation is often very accurate in practical situations, as we will show later in this paper.

C. Normalized Coupled Wave Equations

For the purposes of analysis and numerical simulations, it is often useful to normalize Eqs. (5). The photon flux of wave j is proportional to $(n_j/\omega_j)|A_j|^2$. Motivated by energy conservation, and in particular by the Manley–Rowe relations, we introduce dimensionless envelopes a_j whose square magnitudes are proportional to these photon fluxes. These envelopes are implicitly defined with

$$A_j = \sqrt{\frac{\omega_j}{n_j}}\sqrt{\sum_n \frac{n_n}{\omega_n}|A_{n0}|^2}a_j. \tag{9}$$

In these definitions, A_{n0} is the envelope of wave n at the input to the grating. With these definitions, Eqs. (5) become

$$\frac{da_i}{dz} = -ig(z)\gamma a_s^* a_p e^{-i\phi_1(z)}, \tag{10a}$$

$$\frac{da_s}{dz} = -ig(z)\gamma a_i^* a_p e^{-i\phi_1(z)}, \tag{10b}$$

$$\frac{da_p}{dz} = -ig(z)\gamma a_i a_s e^{+i\phi_1(z)}, \tag{10c}$$

where $g(z) = \sin(\pi D(z))$, and the coupling coefficient γ is given by

$$\gamma = \sqrt{\frac{\omega_i\omega_s\omega_p}{n_i n_s n_p}}\sqrt{\sum_j \frac{n_j}{\omega_j}|A_{j0}|^2}\frac{2d_0}{\pi c}. \tag{11}$$

$\phi_1(z)$ is defined in Eq. (7). The input conditions for Eqs. (10) satisfy, in all cases,

$$\sum_j |a_j(z_i)|^2 = 1. \tag{12}$$

Furthermore, we could also introduce a dimensionless propagation coordinate $\zeta = \gamma z$; however, for clarity we work with physical units instead. An analogous set of normalized CWEs could be obtained, accounting for the full spatial dependence of the QPM grating [$\bar{d}(z) = \pm 1$]. The only differences would be substituting $g(z) \to \pi\bar{d}(z)/2$, and $\phi_1(z) \to \Delta k_0 z$ [see Eqs. (1)].

3. LOW-GAIN, LOW-DEPLETION DEVICES

To begin our study, we first consider cases in which only the generated idler wave in Eqs. (10) changes substantially; the other two envelopes propagate linearly, i.e., without depletion, amplification, or nonlinear phase shifts, and hence are constant. This type of configuration, while quite simple, is applicable to many different types of devices, and can help guide intuition for more complicated cases. We will always assume in this paper that one of the waves is zero at the input of the grating. For definiteness we choose this to be the idler wave, but our results apply to other cases, with minor modifications.

The generated wave, found by integrating Eq. (1a), can be expressed as

$$A_i(z_f) = -i\frac{\omega_i d_0}{n_i c}A_s^* A_p F[\bar{d}(z)](\Delta k_0), \tag{13}$$

where the $\mathcal{F}$ denotes the Fourier transform, defined as $\mathcal{F}[f(z)](k) = \int_{-\infty}^{\infty} f(z)\exp(-ikz)\mathrm{d}z$. Eq. (13) holds for arbitrary QPM structures, for which $\bar{d}(z) = \pm 1$ within the interval $[z_i, z_f]$ and $\bar{d}(z) = 0$ elsewhere. An important consequence of this Fourier transform relation is that in a device of finite length, the idler spectrum acquires a ripple, due to interference associated with the abrupt changes in $\bar{d}(z)$ at z_i and z_f. The same argument applies if we consider only the first Fourier order of the grating, as in Eqs. (5) and (10). In Section 4, we discuss apodization functions to suppress such spectral ripples. In this section, we show solutions for the particular case of a linearly chirped QPM grating, and use that solution to introduce a heuristic for constructing apodization functions for general chirped QPM gratings.

A. Analytical Solution

For a linearly chirped grating, given by $K_g(z) = K_g(z_i) - \Delta k'(z - z_i)$ for constant chirp rate $\Delta k'$. In this case, the phase $\phi_1(z)$ in Eqs. (10) is given by

$$\phi_1(z) = \phi_1(z_i) + \frac{\Delta k'}{2}[(z - z_{\mathrm{pm}})^2 - (z_i - z_{\mathrm{pm}})^2], \tag{14}$$

where z_{pm} is the phasematched point, satisfying $K_g(z_{\mathrm{pm}}) = \Delta k_0$. Assuming $\phi_1(z_i) = 0$ and a constant QPM duty cycle [$g(z) = g_0 =$ constant for $z_i \le z \le z_f$], we integrate Eq. (10a) to obtain a normalized output idler field under the first order QPM approximation. The result is

$$\begin{aligned} a_i(z) = -\frac{1}{2}a_s^* a_p e^{i\pi/4}e^{i\Delta k'(z_{\mathrm{pm}}-z_i)^2/2}\sqrt{\frac{2\pi\gamma^2 g_0^2}{\Delta k'}} \\ \times\left[\mathrm{erf}\left(\sqrt{2}e^{i\pi/4}\sqrt{\Delta k'}(z_{\mathrm{pm}} - z_i)\right)\right. \\ \left.+\mathrm{erf}\left(\sqrt{2}e^{i\pi/4}\sqrt{\Delta k'}(z - z_{\mathrm{pm}})\right)\right], \end{aligned} \tag{15}$$

where erf is the error function. Based on Eq. (15), the generated idler (at $z = z_f$) exhibits a significant ripple in amplitude and phase as a function of z_{pm}, and hence as a function of phase mismatch Δk_0 (based on the mapping between Δk_0 and z_{pm}), and thus on optical frequency ω (based on the mapping between Δk_0 and ω). A mathematically simple way to suppress this ripple is by extending the QPM grating length L to infinity, i.e., $z_i \to -\infty$ and $z_f \to +\infty$. In these limits, the (asymptotic) output idler field is given by

$$a_i^{(L\to\infty)} = \left\{ -i\sqrt{\frac{2\pi\gamma^2 g_0^2}{|\Delta k'|}} e^{-i\pi\,\mathrm{sgn}(\Delta k')/4} e^{\left[i\frac{\Delta k'}{2}(z_{\mathrm{pm}}-z_i)^2\right]} + \frac{\gamma g_0}{\Delta k_1(z_f)} e^{\left[i\frac{\Delta k'}{2}((z_{\mathrm{pm}}-z_i)^2-(z_f-z_{\mathrm{pm}})^2)\right]} - \frac{\gamma g_0}{\Delta k_1(z_i)} \right\} a_s^* a_p, \tag{16}$$

where $\Delta k(z_f)^{-1} \to 0$ as $z_f \to \infty$, and similarly $\Delta k(z_i)^{-1} \to 0$ as $z_i \to -\infty$. The second and third terms in this equation, whose phase oscillates rapidly compared to that of the first term, eventually vanish, yielding a magnitude that is independent of z_{pm} (and hence frequency). In this case, the nonlinear interaction is turned on and off smoothly by the gradual transition from large to small phase mismatch; the result is an apodized interaction.

Further insight can be gained by examining Eq. (10a). In the case of a constant grating duty cycle and a constant, finite phase mismatch, Eq. (10a) supports idler eigenmodes: solutions whose magnitude is independent of z. We define these eigenmodes in the general case [with varying $g(z)$ and $\Delta k(z)$, but still maintaining the assumption of constant signal and pump envelopes] as

$$a_i^{(\mathrm{eig})}(z) = \frac{\gamma g(z)}{\Delta k_1(z)} a_s^* a_p e^{-i\phi_1(z)}. \tag{17}$$

If $\Delta k(z)$ and $g(z)$ are constant, this eigenmode is a solution to Eq. (10a). Based on Eq. (16), we also define the "zeroth-order" idler as $a_i^{(0)} = -i\sqrt{2\pi\gamma^2 g_0^2/|\Delta k'|}\, a_s^* a_p e^{-i\pi\,\mathrm{sgn}(\Delta k')/4}$. With these definitions, Eq. (16) can be written in the following form:

$$a_i^{(L\to\infty)}(z_f) = a_i^{(0)} e^{-i\phi_1(z_{\mathrm{pm}})} + a_i^{(\mathrm{eig})}(z_f) - a_i^{(\mathrm{eig})}(z_i), \tag{18}$$

with spectral ripples essentially originating from the nonzero values of the idler eigenmode at the input and output ends of the device ($a_i^{(\mathrm{eig})}(z_i)$ and $a_i^{(\mathrm{eig})}(z_f)$, respectively). This form usually applies even for gratings with monotonic but spatially varying chirp rates and can, in these more general cases, be understood via the stationary phase approximation [34]. Apodization can thus be viewed as reducing the magnitude of idler eigenmode to zero (or close to zero) sufficiently slowly. The connection between eigenmodes of the TWM interaction and apodization is quite general, and even applies for other, more complicated types of interactions [7], as we discuss in Section 7. Such eigenmodes are also connected with the cascaded phase shifts acquired during phase mismatched $\chi^{(2)}$ interactions [35]. To illustrate Eq. (18) and its accuracy, we show in Fig. 1 the propagation of the idler as a function of z for a particular linearly chirped grating.

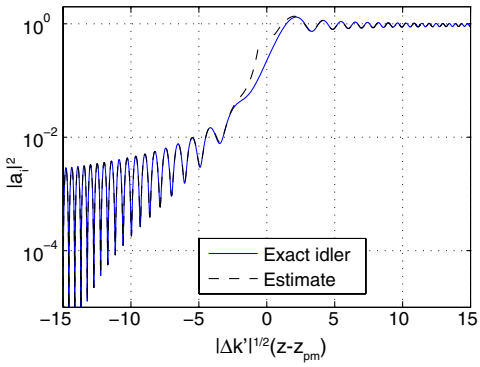

Fig. 1. Evolution of the idler a_i in a linearly chirped QPM grating, for a DFG interaction. The solid (blue) line shows the numerical solution of Eq. (10a), corresponding to (and indistinguishable from) the analytical solution given by Eq. (15). The dashed (black) line shows the asymptotic solution corresponding to Eq. (18). A normalized propagation coordinate, given by $\xi = \sqrt{|\Delta k'|}(z - z_{\mathrm{pm}})$, is used. The idler in each curve is normalized to $|a_i^{(0)}|^2$ [defined by Eqs. (16) and (18)]. The dashed (black) curve shows $[a_i^{(\mathrm{eig})}(z) - a_i^{(\mathrm{eig})}(z_i)]$ for $\xi < -0.5$, and $[a_i^{(\mathrm{eig})}(z) - a_i^{(\mathrm{eig})}(z_i) + a_i^{(0)} \exp(-i\varphi_1(z_{\mathrm{pm}}))]$ for $\xi > 0.5$. The input, phasematching, and output points correspond to $\xi = -15$, $\xi = 0$, and $\xi = 15$, respectively. Because of the way the figure has been normalized, there are no other free parameters in the calculation.

B. Adiabaticity Heuristic

In this subsection, we will use Eqs. (17) and (18) to develop a heuristic criterion by which apodization profiles can be constructed. These apodization regions will be appended to the ends of a nominal grating profile (e.g., linearly chirped); we illustrate different types of apodization in Section 4.

The essential idea is to impose changes in $g(z)$ and $\Delta k_1(z)$ such that the ratio $g(z)/|\Delta k_1(z)| \ll 1$ at $z = z_i$ and $z = z_f$, and for this change to be slow enough that the idler eigenmodes Eq. (17) are still accurate local solutions to Eq. (10a). Inspecting Eq. (17), away from z_{pm}, the eigenmodes have a slowly varying amplitude and rapidly varying phase. Our heuristic is to maintain this structure (phase varying much more rapidly than relative changes in amplitude), which leads to the condition

$$\left| \left(\frac{\gamma g}{\Delta k_1}\right)^{-1} \frac{d}{dz}\left(\frac{\gamma g}{\Delta k_1}\right) \right| \ll \left| \frac{d}{dz}(e^{-i\phi_1}) \right|. \tag{19}$$

In a QPM device supporting a wide spectral bandwidth, this condition must be met for all the spectral components of interest, and hence for all values of z_{pm}, at all positions z within both the input and output apodization profiles. Evaluating the derivatives in Eq. (19) and replacing the $\ll$ by $\le\epsilon$ for "small" $\epsilon > 0$, we thus find, within the apodization regions,

$$\max_{\omega}\left\{ \left| \frac{1}{g}\frac{dg}{dz} - \frac{1}{\Delta k_1}\frac{d\Delta k_1}{dz} \right| - \epsilon|\Delta k_1| \right\} \le 0, \tag{20}$$

where maximization with respect to ω is performed over the spectral range of interest. This equation can be used to construct differential equations for apodization profiles in which $K_g(z)$, $g(z)$, or both, or a related quantity, are varied nonlinearly with position. In Section 4, we consider specific apodization examples based on this adiabaticity equation.

$$K_g(z) = \begin{cases} K_- + [\epsilon s_c(z - z_{b,-}) + (K_{b,-} - K_-)^{-1}]^{-1} & \text{for } K_g(z) < K_{b,-}. \\ K_{\text{nom}}(z) & \text{for } K_{b,-} \le K_g(z) \le K_{b,+}. \\ K_+ + [\epsilon s_c(z - z_{b,+}) + (K_{b,+} - K_+)^{-1}]^{-1} & \text{for } K_g(z) > K_{b,+}. \end{cases} \tag{25}$$

4. QPM APODIZATION TECHNIQUES

In this section, we use Eq. (20) to construct apodization regions for nominally chirped QPM devices, and compare different apodization techniques. We assume that there is a nominal, unapodized chirp profile $K_{\text{nom}}(z)$ that has already been chosen, and show how to determine apodization profiles that are appended to the ends of this nominal profile in order to suppress the spectral ripples that would otherwise occur.

A. Nonlinear Chirp (NLC) Apodization

First, we consider nonlinear chirp apodization (NLCA). In this case, there is a constant duty cycle, $dg/dz = 0$, but a spatially varying chirp rate $d\Delta k_1/dz$. Therefore, Eq. (20) can be written as

$$s_c \frac{dK_g}{dz} = \epsilon \min_{\omega}\{[\Delta k_0(\omega) - K_g(z)]^2\}, \tag{21}$$

where $s_c = -\text{sgn}(\Delta k')$ is the sign of the grating chirp rate, and we have replaced the $\le$ with $=$ (assuming that the inequality is strict for the extrema of the spectrum). Eq. (21) can be expressed in a more explicit form by distinguishing between the input and output ends of the grating, and by treating K_g as the integration variable rather than z (which is possible since we assume monotonic chirp functions):

$$s_c \frac{dK_g}{dz} = \begin{cases} \epsilon[K_- - K_g]^2 & \text{if } \Delta k(z,\omega) > 0, \\ \epsilon[K_+ - K_g]^2 & \text{if } \Delta k(z,\omega) < 0, \end{cases} \tag{22}$$

where $K_- = \min_\omega[\Delta k_0(\omega)]$ and $K_+ = \max_\omega[\Delta k_0(\omega)]$ (with min and max performed over the frequency range of interest). Within each apodization region, Eq. (22) can be solved analytically, yielding the following implicit equation:

$$\frac{1}{K_g(z) - K_\pm} - \frac{1}{K_{b,\pm} - K_\pm} = \epsilon s_c(z - z_{b,\pm}), \tag{23}$$

where $z_{b,\pm}$ and $K_{b,\pm}$ represent boundary conditions. These boundary conditions can be determined from the fact that we append apodization regions to a nominal QPM profile, under the assumption that K_g and dK_g/dz must be continuous at the apodization boundaries. These boundaries are therefore the points at which the chirp rate in Eq. (22) equals the nominal chirp rate. Explicitly, for a nominal profile $K_{\text{nom}}(z)$ and chirp rate $dK_{\text{nom}}/dz \equiv K_{\text{nom},z}$, $z_{b,\pm}$ and $K_{b,\pm}$ are the solutions to the following equations:

$$K_{\text{nom},z}(z_{b,\pm}) = \epsilon s_c[K_\pm - K_{b,\pm}]^2, \tag{24a}$$

$$K_{b,\pm} = K_{\text{nom}}(z_{b,\pm}). \tag{24b}$$

Given the solution to Eq. (24), we can now specify the full form of the grating:

Note that the equation for $K_g(z)$ in the apodization regions diverges with respect to z. Therefore, for a real grating, initial and final values of $K_g(z)$ must be chosen. In choosing these values, we must bear in mind that the final values of $\gamma(\omega)g(z)/\Delta k_1(z,\omega)$ determine the fidelity of the apodization, but only to the extent that the first order QPM contribution ($m = 1$) dominates. The existence of other QPM orders means that, eventually, increases in Δk no longer suppress spectral ripple. In an extreme case of $K_g(z)$ passing through phase-matching for third-order QPM, for example, the spectral ripple could actually be made worse. The limits on $K_g(z)$ are thus determined by a trade-off between apodization fidelity, fabrication constraints, higher-order-QPM contributions, and potentially other issues as well. We expect that in most practical cases, these issues will not substantially limit the performance of the apodized device. Note also that, in a practical device, it may be useful to reduce the chirp rate at the edges of the grating so that the range of $K_g(z)$ is not sensitive to changes in crystal length that occur during polishing. We discuss this further in Subsection 8.B.

In Subsections 4.B and 4.C, we discuss two other apodization techniques. In Subsection 4.D, we show example apodization profiles and corresponding idler spectra (Fig. 2).

B. Duty Cycle Apodization

Another approach to suppressing spectral ripples is by apodizing $g(z)$ instead of Δk_1. In principle, changes in $g(z)$ can be implemented via changes in the QPM duty cycle $D(z)$. Therefore, we refer to this approach as duty cycle apodization (DCA). For this case, we can again assume a known, nominal chirp function (e.g., a linear chirp), and substitute this function into Eq. (20). Analogously to Eq. (21), we find the following differential equation for $g(z)$, suitable for a finite and monotonic nominal chirp rate:

$$s_{g'} \frac{1}{g}\frac{dg}{dz} = \min_{\omega}\left\{ -s_{g'} \frac{1}{\Delta k_0(\omega) - K_g(z)} \frac{dK_g}{dz} \times \left[1 - \sqrt{1 + \epsilon^2 \frac{(\Delta k_0 - K_g(z))^4}{(dK_g/dz)^2}}\right]\right\}, \tag{26}$$

where $s_{g'} = \text{sgn}(dg/dz)$. This equation can be used to determine $g(z)$ in a similar way to the NLCA case discussed in Subsection 4.A, but we omit the mathematical details here.

C. Deleted Domain Apodization

In lithographic poling, it is often challenging in practice to obtain a custom duty cycle function, due to the dynamics of the poling process [30], particularly for MgO:$LiNbO_3$ poling [36]. Instead, the voltage waveform used for poling is usually chosen to yield as close to a 50% duty cycle as possible. Such gratings are also advantageous in order to suppress photorefractive

effects [31], including recently identified pyroelectrically induced beam distortions [32,33].

If duty cycle modulation is not possible, a continuously varying first order QPM coefficient $g(z)$ cannot be achieved. An alternative approach is to use a discrete approximation to the desired continuous $g(z)$ profile, as demonstrated in [24]. In this scheme, QPM domains are "deleted" (not inverted) in order to reduce the effective duty cycle of the grating, averaged over many periods. Therefore, we call this approach deleted domain apodization (DDA). To express this approach mathematically, we assume that the grating has N periods with center positions z_n and length $l_n (n = 1, \ldots, N)$, and either 50% ($g_n = 1$) or 0% ($g_n = 0$) duty cycle. The spatial profile of the grating is then given by

$$\bar{d}(z) = 1 - \sum_n 2 g_n \Pi_{l_n/2}(z - z_n), \tag{27}$$

where $\Pi_l(z)$ is the rectangle function (with width l and center 0). The integral of $(1 - \bar{d})$ should then be a good approximation to the target profile $g(z)$:

$$\sum_n g_n \int_{z_i}^{z} 2\Pi_{l_n/2}(z' - z_n)\mathrm{d}z' \approx \int_{z_i}^{z} g(z')\mathrm{d}z'. \tag{28}$$

A simple way to obtain each g_n from this approximate relation is to initially assume $g_n = 1$, and then reverse the sign of g_{n+1} whenever, for a position $z \approx z_n + l_n/2$, the left hand side of Eq. (28) exceeds the right hand side.

D. Comparison and Discussion

In this subsection, we compare the three apodization techniques described in Subsections 4.A–4.C (NLCA, DCA, and DDA, respectively). We choose an example with the following parameters. The grating center spatial frequency $K_{g0} = 3 \times 10^2$ mm^{-1} (≈21 μm period), nominal length $L_{\mathrm{nom}} = 10$ mm, nominal bandwidth $\Delta k_{\mathrm{BW}} = 20$ mm^{-1}, and positive chirp rate $\Delta k' = +\Delta k_{\mathrm{BW}}/L_{\mathrm{nom}} = 2$ mm^{-2}. Apodization profiles are found via the preceding differential equations, and we choose $\epsilon = 0.5$ in each case (for $\epsilon > 1$, the apodization fidelity decreases). For the NLCA example, the range of k-vectors, $|K_g(z_f) - K_g(z_i)| = 200$ mm^{-1}, and the apodized grating length is $L = z_f - z_i = 14$ mm. For the DCA and DDA examples, $g(z_f) = g(z_i) = 0.052$, and the apodized grating length is $L = z_f - z_i = 16$ mm. The resulting idler spectrum for phase mismatches in the vicinity of first order QPM is shown in Fig. 2. The NLCA profile is found according to Eq. (25); the DCA profile according to Eq. (26), and the DDA example is determined from the DCA profile combined with Eq. (28).

The NLCA and DCA cases show the best ripple suppression, while the DDA case still has a substantial ripple in this example. The NLCA ripple is limited by the range of QPM periods and presence of higher order QPM terms. In cases where precise control of the duty cycle is not possible over a wide range of periods, even orders of the grating will contribute as well, so second-order QPM contributions represent one possible limiting factor for the NLCA approach. These issues are difficult to quantify in general, so we have restricted the example to a range of $K_g(z)$ far from higher-order QPM. The DCA ripple will be limited by the range of duty cycles that can be fabricated reliably. This range is typically quite restricted,

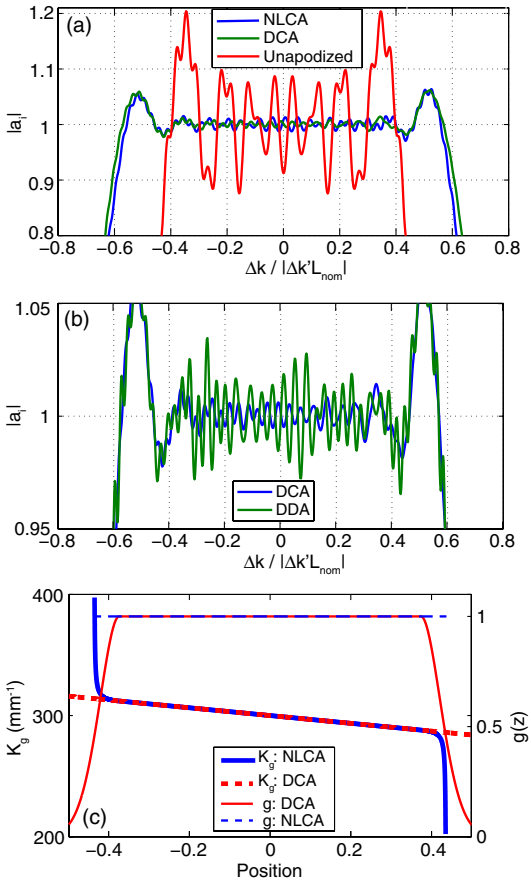

Fig. 2. Apodization examples for DFG, calculated numerically via Eq. (1a), using the full $\bar{d} = \pm 1$ grating structure. (a) Nonlinear chirp apodization (NLCA), (b) duty cycle apodization (DCA), (c) deleted domain apodization (DDA) with a domain profile determined from the DCA example in (b). The parameters are given in the text.

and therefore the high performance of the DCA example may not be achievable in practice. Furthermore, the length of the apodization region will usually be longer for DCA compared with NLCA.

While DDA is not limited by duty cycle fabrication issues, the DDA example exhibits poorer performance than DCA, due to the non-negligible k-space bandwidth, compared to the nominal grating k-vector. Consequently, the implicit assumption of a small change in relative phase between the idler and its driving polarization between the remaining undeleted domains does not hold. More specifically, to achieve a low effective nonlinearity, there must be a large gap between undeleted domains. Since all of the spectral components of interest are phase mismatched in the apodization regions for a chirped grating, this gap can correspond to a large relative phase shift between the idler and its driving polarization. Such large phase shifts likely prevent the interference that would, for the case of a smooth duty cycle modulation, (almost) completely suppress the input and output eigenmodes (and hence the spectral ripples). This issue is particularly important for gratings with a broad k-space bandwidth, such as the example shown in Fig. 2. On the other hand, for periodic QPM gratings, such as those discussed in [24], the underlying assumption of a slowly varying relative phase holds very well, and DDA is effective in such cases.

Since DCA is challenging in terms of fabrication and DDA exhibits reduced performance, the NLCA approach will be favorable in most chirped QPM-grating cases. These conclusions are especially valid in more complicated interactions involving high gain or pump depletion. An example of the poorer performance of DDA compared with NLCA in a high-gain interaction is shown in Section 5.

In each of the above apodization approaches, the absolute scale of the amplitude ripple remaining in the apodized device is determined by fabrication and QPM constraints, such as the presence of higher-order QPM contributions, and is independent of grating length. In contrast, the scale of the "zeroth-order" term [$a_i^{(0)}$ in Eq. (18)] increases with grating length for a given bandwidth, since in a longer device the chirp rate can be reduced. Therefore, the relative scale of the ripples is reduced in longer devices. Note, however, that the range of group delays associated with any remaining spectral ripples is not reduced, and may increase.

5. OPTICAL PARAMETRIC AMPLIFICATION

We now turn our attention to high-gain and high-efficiency devices. In this section, we consider chirped QPM OPA. Such devices have several advantageous properties, including the potential for high gain, almost arbitrary gain bandwidth, tailorable gain and phase spectra, and high conversion efficiency [1,4,5,7]. They have been used in a mid-infrared OPCPA system, enabling broad bandwidth, high power, and high-repetition rate operation [9,10].

A critical consideration in obtaining high-fidelity amplification from these devices is apodization. Without apodization, there is a pronounced ripple in gain and phase; this ripple can be much more severe than in the linear cases (e.g., DFG), due to the high gain involved. The presence of such a ripple can be explained heuristically by the abrupt turn-on and turn-off of nonlinear coupling between the signal and idler fields at the edges of the device, in analogy to the simpler case of DFG. Here, we build on the theoretical work presented in [1] to show how optimal OPA apodization profiles can be constructed. Our approach is similar in spirit to the one presented in Section 4 for DFG apodization.

A. Overview of Chirped QPM OPA

We first give a brief theoretical description of chirped QPM OPA interactions, under the assumption of a cw (or quasi-cw) pump wave, which is undepleted and much stronger than the signal and idler waves ($|a_i| \ll |a_p|$ and $|a_s| \ll |a_p|$). In this case, the amplification of each signal spectral component (and corresponding idler component) is governed by Eqs. (10a) and (10b). By defining new envelopes b_j according to $a_j(z) = g(z)^{1/2}\exp[-i\phi_1(z)/2]b_j(z)$ for $j = i$ and $j = s$, the following second-order equation can be obtained from Eqs. (10a) and (10b) [1]:

$$\frac{d^2 b_s}{dz^2} + Q(z) b_s, \tag{29}$$

where the "potential" $Q(z)$ is given by

$$Q = -(\gamma g)^2 + \frac{1}{2}\frac{d}{dz}\left(\frac{g'}{g}\right) - \frac{i\Delta k'}{2} - \frac{1}{4}\left(\frac{g'}{g} - i\Delta k\right)^2, \tag{30}$$

where $f' = df/dz$ for function $f(z)$. This potential is position dependent (via $g(z)$ and $K_g(z)$) and frequency dependent (via $\gamma(\omega)$ and $\Delta k_0(\omega)$).

Equation (29), which is in standard form, is amenable to complex Wentzel–Kramers–Brillouin (WKB) analysis. This analysis yields several important results for device operation [1]. In particular, for smoothly chirped gratings, the signal intensity gain can be approximated according to

$$\ln(G_s(\omega)) \approx 2\int_{z_i}^{z_f} \mathrm{Re}\sqrt{[g(z)\gamma(\omega)]^2 - \left[\frac{\Delta k_0(\omega) - K_g(z)}{2}\right]^2}\,dz, \tag{31}$$

which, in the case of a constant grating chirp rate ($\Delta k' = \partial\Delta k/\partial z$) and a 50% duty cycle ($g = 1$), yields $G_s = \exp(2\pi\gamma^2/|\Delta k'|)$ for spectral components within the gain bandwidth. Equation (31) shows that gain occurs for each spectral component ω over the spatial region for which the signal-idler coupling, $g(z)\gamma(\omega)$, is sufficiently large compared with the phase mismatch, $\Delta k(z,\omega) = \Delta k_0(\omega) - K_g(z)$. Outside this spatial region, the signal and idler waves are oscillatory. The points where the integrand in Eq. (31) is zero are called turning points. The gain bandwidth can be determined from Eq. (31) as the range of frequencies for which both turning points lie within the grating. For the case of a linear grating chirp, this bandwidth is given implicitly as the range of frequencies ω whose phase mismatch $\Delta k_0(\omega)$ lies within the following range:

$$\left\{\omega : (\Delta k_0(\omega) - K_{g0}) \in \left[-\frac{|\Delta k' L|}{2} + 2\gamma(\omega), +\frac{|\Delta k' L|}{2} - 2\gamma(\omega)\right]\right\}, \tag{32}$$

for center grating k-vector K_{g0}.

Outside the gain region, the waves are oscillatory versus position, leading to fluctuations of the output waves versus frequency, and consequently a ripple in the output spectrum (since the oscillations of different spectral components have different phase). These properties are illustrated in Fig. 3, where we show the propagation of a single spectral component. The figure shows both an unapodized and an apodized case. Apodized and unapodized gain spectra are shown later, in Fig. 4, after we have discussed an apodization scheme.

B. Apodization Constraint for Chirped QPM OPA

The oscillatory behavior shown in Fig. 3 can be understood as interference associated with the two complex WKB global asymptotic solutions of Eqs. (29) (see, for example, the appendices of [1]). The role played by these global solutions in the context of amplitude oscillations is twofold: first, the assumed input conditions to the device (zero idler, finite signal) imply that the signal consists of a complex linear superposition of these two global solutions. Second, the global solutions themselves are oscillatory. Given such oscillations, frequency-dependent changes in the phasematched point lead to oscillations in the gain spectrum.

These spectral oscillations can be suppressed by suppressing oscillations in the WKB solutions, which is achieved by the condition $|\nu(z)| \gg 1$ for $z = z_i$ and $z = z_f$, where ν is defined as

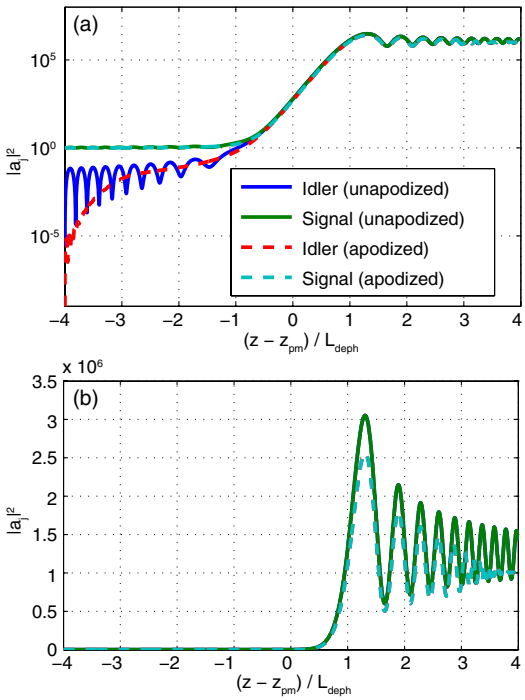

Fig. 3. Propagation example for OPA in a linearly chirped QPM grating, showing the signal and idler as a function of normalized position. The gain factor $\lambda_R = 2.2$. The position has been normalized to the dephasing length, $L_{\text{deph}} = 2\gamma/|\Delta k'|$. The normalized grating length is given by $L/L_{\text{deph}} = 8$. The phasematching point z_{pm} is located at the middle of the grating. The dashed lines show the evolution of the signal and idler in a apodized grating with the same parameters; oscillations in $a_i(z)$ and $a_s(z)$ near $z = z_i$ and $z = z_f$ are suppressed in this case. For this example, we apodize via the chirp rate and duty cycle simultaneously to reveal the idler evolution under idealized input conditions; (b) shows the fields on a linear scale to better indicate how the oscillations are suppressed near the output of the grating in the apodized case, but not the unapodized case; the signal and idler magnitudes are indistinguishable on this linear scale due to the high gain involved.

$$\nu(z) \equiv \frac{\Delta k_1(z)}{2\gamma g(z)}. \tag{33}$$

The $|\nu(z_i)| \gg 1$ condition ensures that the input conditions correspond to one of the two global solutions (very small contribution from the other solution) [Eqs. (C4) and (C5) of [1]]. The $|\nu(z_f)| \gg 1$ condition suppresses ripples on this global solution [Eq. (C3) of [1]].

These conditions are also quite closely related to the idler eigenmodes of Eq. (17). Indeed, for large phase mismatches, Eqs. (10a and 10b) support two *local* signal-idler eigenmodes whose amplitudes would be constant with respect to position in the case of a constant and large phase mismatch and constant duty cycle. These eigenmodes may be determined by substituting $a_i = a_{i0}\exp(i\int_{z_i}^{z}\phi_i(z')\mathrm{d}z')$ and $a_s = a_{s0}\exp(i\int_{z_i}^{z}\phi_s(z')\mathrm{d}z')$ into Eqs. (10a and 10b), neglecting derivatives of $a_{j0}(z)$, and solving for $\phi_i(z)$, $\phi_s(z)$, and $|a_{s0}(z)/a_{i0}(z)|^2$. While these eigenmodes are not solutions to Eqs. (10a and 10b) in the case of a varying phase mismatch, they provide some insight into the more complicated dynamics supported by the WKB solutions described above.

For large phase mismatches, one of these two eigenmodes has a small signal component, while the other has a small idler component. The rate of signal-phase accumulation, $\varphi_s(z)$, differs between these two eigenmodes, leading to amplitude oscillations unless the signal and idler fields correspond to only one of the eigenmodes. In the limit where $\nu(z_i)^{-1} = 0$, the input conditions (zero idler) are matched to one of the two eigenmodes, thereby suppressing ripples near the start of the grating [region $z_i \le z \ll z_{\text{pm}}$ of the apodized example in Fig. 3] since the magnitude of this eigenmode varies slowly as ν is decreased, but does not vary over the fast Δk^{-1} length scale associated with the local phase mismatch Δk. Note that the different length-scales in phase-mismatched TWM interactions have been analyzed using multiple-scale analysis in [37].

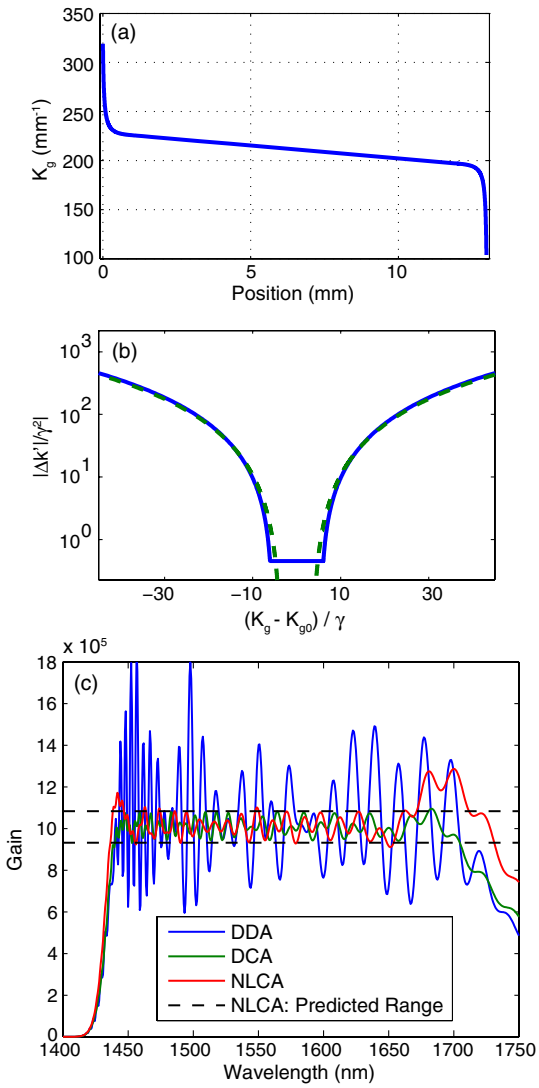

Fig. 4. Chirped-QPM OPA apodization examples. (a) Grating k-vector profile for a NLCA example, (b) normalized grating chirp rate corresponding to (a), and (c) signal gain spectrum. The dashed lines in (b) show $\min((\Delta k_1/\gamma_0)^2)\epsilon$, with minimization performed with respect to signal wavelength (restricted to the target gain bandwidth that spans the 1450–1650 nm range). This figure indicates that the optimal normalized chirp rate in the apodization region approximately satisfies $|\Delta k'| = \min(\Delta k_1^2)\epsilon$. The dashed lines in (c) indicate analytical estimates of the fluctuations in the gain due to the finite value of $|\gamma_0/\Delta k_1|$ at the ends of the grating, as described in the text. The gain spectra for DCA and corresponding DDA examples are also shown in (c), for comparison.

After the amplification region ($z \gg z_{\mathrm{pm}}$), the fields can be thought of as consisting of a linear combination of the two local eigenmodes. In the limit where $\nu(z_f)^{-1} = 0$, the signal-component of one of the two eigenmodes is brought to zero at the end of the grating, thereby suppressing signal-amplitude oscillations [region $z_{\mathrm{pm}} \ll z \le z_f$ of the apodized example in Fig. 3].

The $|\nu(z_i)|^{-1} = 0$ and $|\nu(z_f)|^{-1} = 0$ conditions can be achieved, in principle, by extending the nominal grating chirp profile to infinity. In practice, this condition can be achieved (with high fidelity) by apodization. In performing such apodization, $|\nu(z)|$ in Eq. (33) should be increased slowly enough that the local WKB solutions remain accurate; if $\nu(z)$ is changed too rapidly, there will be coupling between the two asymptotic solutions of Eqs. (10), again leading to interference. As such, a sufficient criterion is to maintain the validity of the WKB approximation within the apodization regions. This condition corresponds, for an individual spectral component ω, to the following inequality [38]:

$$\left| \frac{dQ}{dz} \frac{1}{Q^{3/2}} \right| \le \epsilon, \tag{34}$$

for "small" ϵ. This condition should be maintained for all spectral components of interest [i.e., all within the amplification bandwidth associated with Eq. (31)].

C. Nonlinear Chirp Apodization for OPA

In this subsection we use Eq. (34) to determine apodization profiles for undepleted-pump, chirped QPM OPAs. As before, we start from a nominal grating design, such as a linear chirp profile. Apodization regions are then appended to this nominal design, with the grating k-vector and duty cycle properly matched at the joining points. With Eq. (34), these apodization regions can be made as short as possible. This condition will help with meeting any maximum grating length constraints. In the context of OPAs, an even greater benefit is that optimized apodization profiles will ensure that parasitic effects, such as pump SHG and other unwanted processes, can be avoided or suppressed in the apodization regions by having a chirp rate that is as high as possible within as short a length as possible.

Equation (34) yields an implicit differential equation in z which, as stated, is difficult to solve. A much simpler equation is obtained by writing $g(z)$ and the chirp rate $K_z \equiv dK_g/dz$ as functions of K_g, and integrating versus K_g. This approach is possible because we assume that $K_g(z)$ is monotonic, and $g(z)$ is monotonic within each individual apodization region. For notational convenience, in the following analysis we suppress the g subscript on K_g. We mainly consider NLCA rather than DCA or DDA for the reasons discussed in Subsection 4.D, and therefore assume that $g(z)$ is constant versus position. For simplicity, we also assume that $\gamma(\omega) = \gamma_0$ is frequency-independent, although in practice this assumption is not necessary.

With the above assumptions, the following equation can be obtained from Eqs. (30) and (34):

$$\left(\frac{dK_z}{dK}\right)^2 \le \min_{\Delta k_0} \left\{ \frac{4\epsilon^2}{K_z^2} \left| \left(\frac{\Delta k}{2}\right)^2 - \gamma_0^2 + i\frac{K_z}{2} \right|^3 - \Delta k^2 \right\} \equiv \min_{\Delta k_0} \{ f(\Delta k_0, K, K_z) \}, \tag{35}$$

where $\Delta k(z,\omega) = \Delta k_0(\omega) - K(z)$. The minimization in Eq. (35) with respect to $\Delta k_0(\omega)$ is performed over the desired amplification bandwidth of the device. The function f has been introduced as a shorthand to identify the dependence of the inequality on Δk_0 (and hence on optical frequency).

Close to the turning points satisfying $\Delta k_0 - K = \pm 2\gamma_0$, $f(\Delta k_0, K, K_z)$ is negative (unless ϵ is chosen to be too large, e.g., $\epsilon \gg 1$), which means that $|dQ/dz| > \epsilon |Q^{3/2}|$. If we move far enough from these turning points (toward the edges of the nominal grating profile) then equality is obtained. We wish to find a pair of grating k-vectors at which to begin the apodization region; these are denoted $K_{\mathrm{apod},s}$ and $K_{\mathrm{apod},e}$ for the start-regions and end-regions of the grating, respectively. These will be the k-space points at which inequality in Eq. (35) is satisfied for the whole spectral range of interest. The minimization in Eq. (35) will correspond to either the minimum or maximum value of $\Delta k_0(\omega)$ across this spectral range. Beyond these k-vectors, it is possible to chirp the grating more rapidly while still satisfying Eq. (34). We therefore assume that the inverse grating profile, $z(K)$, corresponds to a nominal chirp profile $z_{\mathrm{nom}}(K)$ for K between $K_{\mathrm{apod},s}$ and $K_{\mathrm{apod},e}$, and is determined via Eq. (35) outside this region.

Based on the above discussion, we first determine $K_{\mathrm{apod},s}$ and $K_{\mathrm{apod},e}$ by solving the following pair of equations:

$$\min_{\Delta k_0} \{ f(\Delta k_0, K_{\mathrm{apod},j}, K_{z,\mathrm{nom}}) \} = \left(\frac{dK_{z,\mathrm{nom}}}{dK} \right)^2, \tag{36a}$$

$$\min_{\Delta k_0} [|\Delta k_0 - K_{\mathrm{apod},j}|] \ge 2\gamma_0, \tag{36b}$$

for $j = s$ and $j = e$, where subscript "nom" denotes the nominal grating profile. For a linearly chirped grating, $K_{z,\mathrm{nom}}(K)$ is constant. Eq. (36a) arises from Eq. (35), while Eq. (36b) ensures that the $K_{\mathrm{apod},j}$ lie outside the amplification region for all of the spectral components involved.

It is convenient to define the k-space domain of the nominal grating:

$$\mathrm{dom}(K_{\mathrm{nom}}) = \{ K : \min_j (K_{\mathrm{apod},j}) \le K \le \max_j (K_{\mathrm{apod},j}) \}. \tag{37}$$

We now use $K_{\mathrm{apod},j}$ to find the entire grating profile by first solving the following equations for $K(z)$ and $K_z(K)$:

$$K(z) = K_{\mathrm{nom}}(z), K \in \mathrm{dom}(K_{\mathrm{nom}}), \tag{38a}$$

$$\frac{dK_z}{dK} = s_{K_z} \min_{\Delta k_0} (\sqrt{f}), K \notin \mathrm{dom}(K_{\mathrm{nom}}), \tag{38b}$$

where $s_{K_z} = \mathrm{sgn}(dK_{z,\mathrm{nom}}/dK)$, and with the initial conditions for Eq. (38b) given by

$$K_z(K_{\mathrm{apod},j}) = K_{z,\mathrm{nom}}(K_{\mathrm{apod},j}). \tag{39}$$

Equations (38a) and (38b) yield $K_z(K)$ over the entire grating spatial frequency profile. We can thus determine $z(K)$ by

$$z(K) = \int_{K_i}^{K_f} K_z(K)^{-1} \mathrm{d}K, \tag{40}$$

and then invert this function to find $K_g(z)$.

An example implementation of this design procedure is shown in Fig. 4. For this example, we select a specific experimental configuration. We assume an MgO:$LiNbO_3$ OPA device at 150 °C, designed to amplify signal components between 1450 and 1650 nm using a narrow-bandwidth 1064 nm pump. The corresponding range of idler wavelengths is 3000–4000 nm. For illustration purposes, we assume a nondispersive coupling coefficient γ, with $\gamma(\omega) = \gamma_0$. We choose a gain coefficient $\lambda_{R,p} = \gamma_0^2/|\Delta k'| = 2.2$. The range of phase mismatches corresponding to the signal bandwidth is $\Delta k_{\mathrm{BW}} \approx 16.6\ \mathrm{mm}^{-1}$. This value originates from the material phase mismatches of $\Delta k = 219.7$ and $203.1\ \mathrm{mm}^{-1}$ for signal wavelengths of 1450 and 1650 nm, respectively. According to Eq. (31), a linear chirp rate $\Delta k'$ and nominal grating length L_{nom} satisfying $|\Delta k' L_{\mathrm{nom}}| = \Delta k_{\mathrm{BW}} + 4\gamma_0$ are required in order to fully amplify this bandwidth. Therefore, given values of L_{nom}, Δk_{BW}, and $\lambda_{R,p}$, the values of γ_0 and $|\Delta k'|$ can be determined. Here, we choose $L_{\mathrm{nom}} = 10$ mm, which yields $\gamma_0 \approx 2.4\ \mathrm{mm}^{-1}$ and $\Delta k' = \pm 2.62\ \mathrm{mm}^{-2}$.

To construct an apodization profile, we assume a positive chirp rate ($\Delta k' > 0$), a symmetric grating profile, set $\epsilon = 1$, and solve Eq. (38). It is useful to introduce a parameter δ to describe the range of grating k-vectors,

$$\left| \frac{K_g(z_f) - K_g(z_i)}{2\gamma} \right| \leq \delta, \tag{41}$$

where we choose $\delta = 45$ for the present example. This value is chosen to yield large values of $|\nu|$ defined in Eq. (33) at the ends of the device, while still remaining far from higher-order QPM. For our example, $K_g(z_i) \approx 319.5\ \mathrm{mm}^{-1}$ and $K_g(z_f) \approx 103.3\ \mathrm{mm}^{-1}$.

The k-vector profile is shown in Fig. 4(a). In Fig. 4(b), the grating chirp rate is compared to Δk^2, illustrating that optimal normalized chirp rate is approximately proportional to the square of the minimum phase mismatch. The output gain spectrum as a function of wavelength is shown in Fig. 4(c). We show DCA and DDA examples for comparison to the NLCA case. For each of these simulations, we assume the full grating structure ($\bar{d} = \pm 1$) and integrate Eqs. (1) numerically, for each spectral component, within each successive QPM domain.

The finite value of δ^{-1} defined above as well as higher-order QPM contributions result in a ripple in the gain for the NLCA example. Under the assumption of a first order QPM interaction, the ripple is such that $|\ln(G_s) - 2\pi\lambda_{R,p}| \leq 4\delta^{-1}$ for frequencies within the amplification region [1]. In a real grating, there are also small contributions from the other orders of the QPM grating. The dashed black lines in Fig. 4 are bounds on the gain ripple found by analytically summing *all* such contributions, showing excellent agreement with the full numerical NLCA simulations. The gain spectra for the DCA and DDA examples are also included. The DCA example was specified heuristically, with an amplitude profile determined via hyperbolic tangent functions; it shows comparable performance to NLCA, but requires large modulation of the QPM duty cycle. The DDA example was derived from the DCA example, and shows a significant reduction in apodization quality compared with both DCA and NLCA. For these DCA and DDA examples, the chirp rate is linear. Note that with no apodization, the ripple is huge, with gain varying by a factor of 4 across the passband (from $\approx 0.5 \times 10^6$ to $\approx 2 \times 10^6$).

6. ADIABATIC FREQUENCY CONVERSION

We next consider adiabatic frequency conversion (AFC). This type of interaction can occur in chirped QPM gratings when the coupling between the three waves is sufficiently strong, and enables high pump conversion efficiency across a very broad range of phase mismatches and intensities. In this section, we first show how AFC can be analyzed and understood in general TWM configurations. In Section 7, we develop an apodization procedure for AFC devices via an approach similar to the DFG and OPA cases considered above.

In AFC, instead of reaching a maximum at a certain input intensity, the pump depletion can increase monotonically with respect to the input intensity of either the pump or signal wave, or both [7,8]. Rather than back-convert after the point of maximum pump depletion, the fields adiabatically follow a local nonlinear eigenmode that evolves with the grating period. If the grating is sufficiently chirped, then at the input to the device, the relevant eigenmode corresponds to zero idler (i.e., to the input conditions), while at the output this eigenmode corresponds to zero pump (the desired output condition of full pump depletion). This adiabatic following process is possible provided that the coupling rate γ between the fields is strong enough (at a given chirp rate $\Delta k'$), or if the chirp rate is slow enough (at a given coupling rate). The required coupling rate also depends on the input conditions, as we will discuss.

Before considering AFC and nonlinear eigenmodes in more detail, we discuss in Subsection 6.A a reformulation of Eqs. (10) based on [28], in which TWM interactions are described geometrically. This geometric analysis provides many insights into the structure of various TWM processes, especially AFC, as we will show.

A. Geometric Analysis of Three-Wave Mixing Interactions

In [28], the geometrical analysis was motivated by the Hamiltonian structure of the TWM equations. Furthermore, [28] considered general QPM interactions, corresponding to $\bar{d} = \pm 1$. Here, we briefly recapitulate the formulation given in more detail in [28], and give the modifications required for first order QPM interactions.

First, reduced field variables X, Y, and Z can be defined according to

$$\begin{aligned} X + iY &= a_i a_s a_p^* e^{i\phi_1(z)} \\ Z &= |a_p|^2, \end{aligned} \tag{42}$$

The phase of $X + iY$ specifies the relative phase between the envelopes a_j and their driving polarizations in the CWEs [Eqs. (10)], and hence the direction of energy transfer. The remaining variable Z specifies the pump photon flux. These variables can be treated as specifying a real-valued "position" vector $\mathbf{W}$ in an abstract 3-space, defined as

$$\mathbf{W} = [X, Y, Z]^T. \tag{43}$$

During propagation, $\mathbf{W}$ evolves according to the evolving complex envelopes a_j, but is constrained to lie on a surface whose

shape is determined by the input conditions. This surface is given by the implicit relation $\varphi = 0$, where

$$\varphi = X^2 + Y^2 - Z(Z - K_{\mathrm{ip}})(Z - K_{\mathrm{sp}}), \tag{44}$$

and where the constants K_{ip} and K_{sp} are Manley–Rowe invariants, given by

$$K_{jp} = |a_j|^2 + |a_p|^2, \tag{45}$$

for $j = i$ and $j = s$. With the envelope definitions and input conditions considered here, with zero input idler, $K_{\mathrm{sp}} = 1$ and $K_{\mathrm{ip}} = |a_p(z_i)|^2 \le 1$. It is convenient to introduce a parameter ρ describing the ratio of input photon fluxes: $\rho \equiv |a_s(z_i)/a_p(z_i)|^2$. For cases with an input signal that is much larger than the pump ($\rho \gg 1$, and hence $0 \le Z \le K_{ip} \ll 1$), $\varphi = 0$ is (approximately) a sphere. For other input conditions ($\rho \not\gg 1$), the conserved surface $\varphi = 0$ is not spherical, but remains closed and convex [28].

The evolution of W is given by

$$\frac{d\mathbf{W}}{d(\gamma z)} = \nabla H \times \nabla \varphi, \tag{46}$$

where $\nabla = [\partial/\partial X, \partial/\partial Y, \partial/\partial Z]^T$, and where the local Hamiltonian H, which is discussed in more detail in [28], can be expressed as

$$H = gX + \frac{\Delta k}{2\gamma}(Z - (K_{\mathrm{ip}} + K_{\mathrm{sp}})). \tag{47}$$

This local Hamiltonian is position-dependent in the case of a chirped QPM grating. Eq. (46) implies that $\mathbf{W}$ is constrained to remain on the implicit surface $\varphi = 0$, since the "force" acting on $\mathbf{W}$ is perpendicular to the local surface normal $\nabla\varphi$.

B. Solution for Uniform QPM Gratings

The geometrical approach of [28], an important result of which is reproduced in Eq. (46), greatly simplifies the interpretation of many TWM problems. For example, during propagation in a uniformly phasematched medium, $\mathbf{W}$ is constrained to lie on the intersection between a plane ($H =$ constant) and a convex surface ($\varphi = 0$), and hence on a ring (or a single point). The distance required to fully traverse the ring is the period associated with the Jacobi-elliptic analytical solutions of the there-wave mixing problem, derived in [39]. Much of the complicated structure of these analytical solutions can thus be visualized with this geometrical construction.

Furthermore, Eq. (46) reveals the existence of the local nonlinear eigenmodes discussed above. The existence of such eigenmodes is well known [35], but the geometric description provides a particularly convenient framework for their study, and the interpretation of their role in spatially nonuniform structures, such as chirped gratings.

These eigenmodes, which we denote as $\mathbf{W}_m$, satisfy $d\mathbf{W}/dz = 0$, and hence correspond to the two points for which ∇H is normal to the surface $\varphi = 0$ (the points where $\nabla\varphi$ is in the same direction as $\pm\nabla H$). Because $\varphi = 0$ is closed and convex, there are two and only two such points. These eigenmodes can also be viewed as generalizations of the eigenmodes we discussed in Subsections 3.A and 5.B for the specific cases of DFG and OPA, respectively.

To illustrate the nonlinear eigenmodes and the evolution of $\mathbf{W}$, we show in Fig. (5) a propagation example for a uniformly phasematched device. In this example, the black arrow points in the direction of ∇H; its location has been chosen so that the point where it touches the conserved surface $\varphi = 0$ corresponds to a nonlinear eigenmode. Since the medium is uniform (constant g and Δk_1, and other QPM orders are neglected), this eigenmode is fixed, and hence represents a true eigenmode of the TWM interaction. In a chirped device, the direction of ∇H, and hence the local nonlinear eigenmode $\mathbf{W}_m$, would be swept from the top to the bottom of $\varphi = 0$ as $\nu = \Delta k_1/(2\gamma g)$ [see Eq. (33)] is swept from $\pm\nu \gg 1$ to $\mp\nu \gg 1$.

C. Solution for Chirped QPM Gratings

We next consider the AFC solutions supported by chirped QPM gratings, for which the reduced field vector $\mathbf{W}(z)$ can follow the nonlinear eigenmodes $\mathbf{W}_m(z)$. Since $\mathbf{W}_m = [X_m \quad Y_m \quad Z_m]^T$ are points where $\nabla H \times \nabla\varphi = 0$, they can be found, for any given value of ν, by solving the following set of equations:

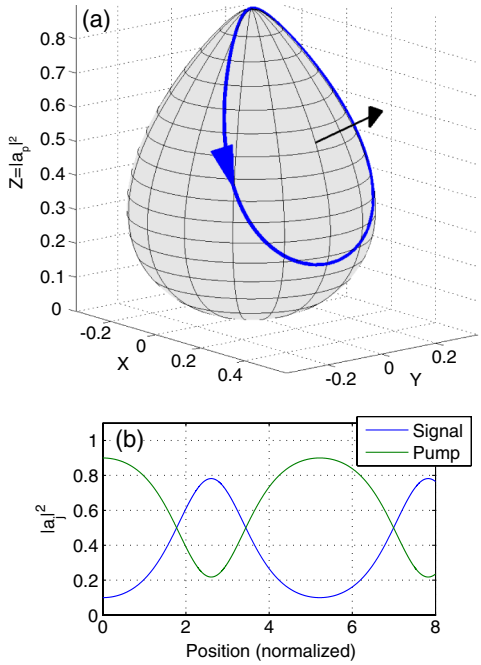

Fig. 5. (a) Solution to an example TWM problem, visualized with the geometric description of [28] [and Eq. (46) in particular]. The parameters for this example are $K_{\mathrm{ip}} = |a_p(z_i)|^2 = 0.9$, $g = 1$ (50% duty cycle), and $\Delta k_1/\gamma = 1$. The surface shown is $\varphi = 0$, and the curve (blue) represents the trajectory of $\mathbf{W}$. Since Δk_1 and g are both constant in this example, the curve lies on a plane $H =$ constant. $\mathbf{W}$ is initially at the top of the surface ($Z \equiv |a_p|^2 = K_{\mathrm{ip}} = 0.9$), and the direction of $\mathbf{W}$ (with increasing z) is shown by the blue arrow on the curve. The direction of ∇H is also shown (black arrow). The point where this arrow touches the surface is a nonlinear eigenmode associated with the chosen parameters (i.e., a point where ∇H is in the direction of the surface normal to $\varphi = 0$, $\nabla\varphi$). In this unchirped example, the field vector $\mathbf{W}$ orbits around the fixed eigenmode $\mathbf{W}_m$. In (b), the photon fluxes $|a_j|^2$ are shown for comparison. One period of these fluxes corresponds to a complete traversal of the blue curve in (a); position is normalized to γ, defined in Eq. (11).

$$\varphi = 0, \tag{48a}$$

$$\frac{\partial \varphi}{\partial Z} = \nu \frac{\partial \varphi}{\partial X}, \tag{48b}$$

$$Y = 0, \tag{48c}$$

where Eq. (48a) ensures that the eigenmode is consistent with the input conditions, and Eqs. (48b) and (48c) follow from the forms of ∇H and $\nabla \varphi$.

Because $\varphi = 0$ is convex for all input conditions, the eigenmodes always evolve through chirped QPM gratings in a similar way. The relevant nonlinear eigenmode initially corresponds to low idler energy, and is swept smoothly (by changing g and Δk_1) to one corresponding to low pump energy. If the sweep rate is slow enough (conditions for which are discussed in Subsection 7.A), the fields follow this eigenmode, and as a result most of the pump energy is transferred to the signal and idler waves. To parameterize the solutions for linearly chirped gratings, we introduce normalized coupling factors $\lambda_R = \gamma^2/|\Delta k'|$, $\lambda_{R,p} = (1+\rho)^{-1}\gamma^2/|\Delta k'|$, and $\lambda_{R,s} = (1+1/\rho)^{-1}\gamma^2/|\Delta k'|$. For an undepleted-pump OPA ($\rho \to 0$), the signal gain is given by $|a_s(z_f)/a_s(z_i)|^2 = \exp(2\pi\lambda_{R,p})$ [1]. For a constant-signal DFG or SFG interaction ($\rho \to \infty$), the pump depletion is given by $|a_p(z_f)/a_p(z_i)|^2 = \exp(-2\pi\lambda_{R,s})$ [8].

To illustrate the AFC process, we show in Fig. 6 the trajectory of the reduced field vector $\mathbf{W}$ (solid lines) and the local nonlinear eigenmode $\mathbf{W}_m$ (dashed lines) for four example cases, with the following parameters: (b) $\lambda_{R,s} = 1$ and $K_{ip} = 10^{-3}$, (c) $\lambda_{R,s} = 2$ and $K_{ip} = 10^{-3}$, (e) $\lambda_{R,p} = 2$ and $K_{ip} = 0.9$, and (f) $\lambda_{R,p} = 10$ and $K_{\mathrm{ip}} = 0.9$. The structure of $\varphi = 0$ is shown in Figs. 6(a) and 6(d) for the input conditions $K_{ip} = 10^{-3}$ (0.1% of input photons in the pump, 99.9% in the signal) and $K_{\mathrm{ip}} = 0.9$ (90% of input photons in the pump, 10% in the signal), respectively.

For both choices of K_{ip}, the adiabatic following process requires a large coupling factor λ_R; for smaller λ_R, a ripple in the components of $\mathbf{W}$ [solid lines in Figs. 6(b), 6(c), 6(e), and 6(f)]

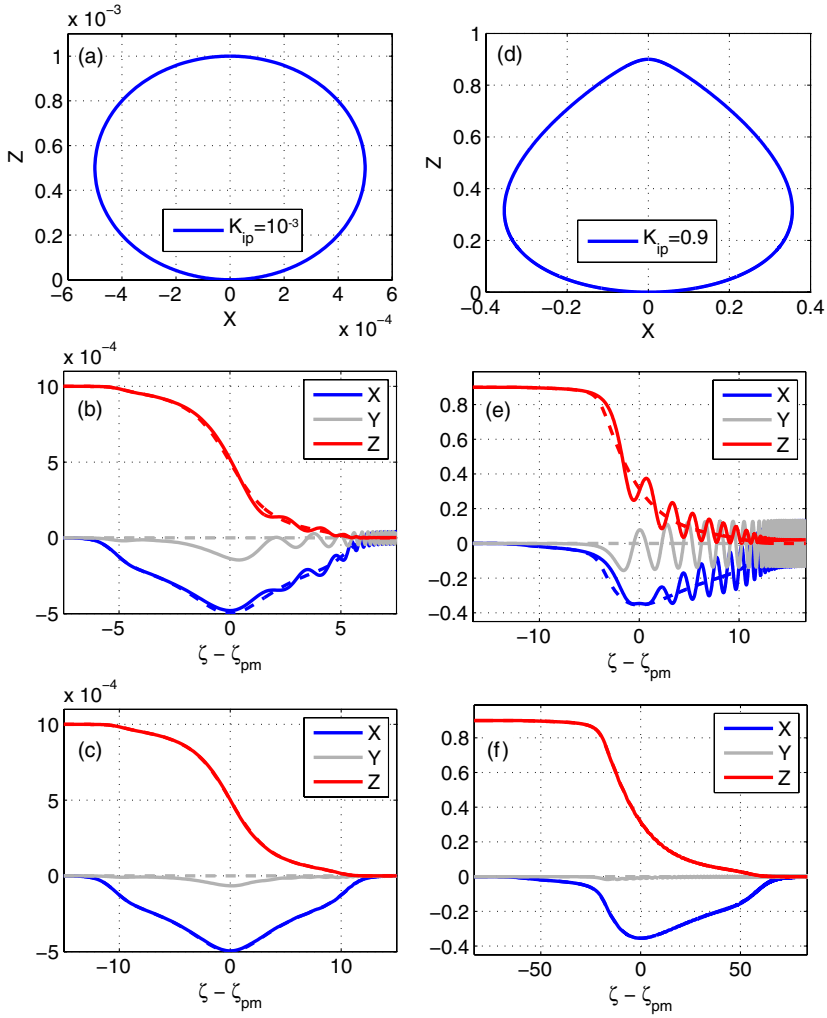

Fig. 6. Propagation of field vector $\mathbf{W}$ and eigenmode vector $\mathbf{W}_m$ [the solid and dashed lines, respectively, in (b), (c), (e), and (f)], illustrating the adiabatic following process arising from Eq. (46). The left column is for $K_{\mathrm{ip}} \equiv |a_p(z_i)|^2 = 10^{-3}$ (strong input signal), while the right column is for $K_{\mathrm{ip}} = 0.9$ (strong input pump). The first row [(a) and (d)] are cuts through the surface $\varphi = 0$ in the plane $Y = 0$, corresponding to these two input conditions. The second and third rows show the evolution of the field vectors (versus coordinate $\zeta = \gamma z$) under these input conditions, for two different coupling factors: $\lambda_{R,s} = (1, 2)$ for (b) and (c), respectively, and $\lambda_{R,p} = (2, 10)$ for (e) and (f), respectively. In (b), (c), (e) and (f), the x curve is on the bottom, y in the middle, and z on the top.

around $\mathbf{W}_m$ (dashed lines) is introduced. Such ripples occur when the chirp rate is too rapid for the fields to follow the local eigenmode; they are thus indications of nonadiabaticity. For the strong-signal case ($K_{\mathrm{ip}} = 10^{-3}$), the amplitude of these ripples scales as $\exp(-2\pi\lambda_{R,s})$; for the strong-pump case ($K_{\mathrm{ip}} = 0.9$) the behavior is more complicated, but a fast decay of the ripple amplitude with respect to $\lambda_{R,p}$ is still obtained at large $\lambda_{R,p}$. At larger values of the coupling factors, the fields $\mathbf{W}$ can be seen in Fig. 6 to follow the local eigenmode $\mathbf{W}_m$ more closely (the ripple amplitude is reduced).

A ripple in $\mathbf{W}(z)$ also occurs if the fields are not launched properly into the input eigenmode, i.e., if $|\nu(z_i)|$ is not large enough: unless $|\nu(z_i)|^{-1} = 0$, the input conditions ($|a_i(z_i)| = 0$) are different from that of the input eigenmode ($|a_i| \neq 0$). These ripples are not noticeable in Fig. 6 because we have introduced an apodization profile to ensure that $|\nu(z_i)|$ and $|\nu(z_f)|$ are very large.

7. ADIABATIC FREQUENCY CONVERSION: APODIZATION

A. Adiabaticity Condition Based on Geometric Picture

The AFC solutions illustrated in Subsection 6.C are obtained for all input conditions provided that the grating is sufficiently chirped, and the chirp rate is sufficiently slow. In order to make use of these solutions in a practical setting, it is important to determine how rapidly the grating can be chirped while still maintaining adiabaticity. In this section, we determine a heuristic constraint for the QPM chirp rate. If this constraint is satisfied, then the adiabatic following process can occur (with a certain fidelity).

As ν is varied (by changing Δk_1, g or both), the local eigenmode $\mathbf{W}_m$ changes, but always remains in the X–Z plane (since $Y_m = 0$). When the reduced field vector $\mathbf{W}$ is in the X–Z plane, each of the envelopes a_j is $\pm\pi/2$ radians out of phase with its driving term in Eq. (10), which implies that $d|a_j|/dz = 0$; this is why $\mathbf{W}_m$ lies in the X–Z plane. Further physical insight into the meaning of this X–Z plane can be gained by considering an unchirped device: $\mathbf{W}$ passes through the X–Z plane at points where the direction of energy flow changes (e.g., at points where the pump is fully depleted, just before the onset of back-conversion).

In order for adiabatic following to occur, the reduced variable Z must keep up with the corresponding component Z_m of the local eigenmode, and hence it is necessary that

$$\frac{dZ}{dz} \approx \frac{dZ_m}{dz}. \tag{49}$$

To satisfy this condition, $\mathbf{W}$ must be sufficiently separated from the X–Z plane: from the form of $d\mathbf{W}/dz$ [Eq. (46)], $dZ/d(\gamma z) = 2gY$, and therefore the required magnitude of Y increases with dZ_m/dz, while dZ_m/dz increases with the chirp rate.

Since $\varphi = 0$ is convex, an angle $\theta_\parallel$ in the X–Z plane associated with the local eigenmode can be defined according to

$$\tan(\theta_\parallel) = \left.\frac{\partial\varphi/\partial Z}{\partial\varphi/\partial X}\right|_{\mathbf{W}=\mathbf{W}_m} = \nu, \tag{50}$$

To see why the latter equality holds, recall that $\nu = \Delta k/(2\gamma g)$, $Y_m = 0$, and that the eigenmodes $\mathbf{W}_m$ are points for which $\nabla\varphi = [\,\partial\varphi/\partial X \quad \partial\varphi/\partial Y \quad \partial\varphi/\partial Z\,]$ is parallel or antiparallel to $\nabla H = [\,g \quad 0 \quad \Delta k/(2\gamma)\,]$. Based on the curvature of $\varphi = 0$, an angle $\theta_\perp$ associated with the value of Y can be defined according to

$$Y = R_\perp(\mathbf{W}_m)\sin(\theta_\perp), \tag{51}$$

where $R_\perp$ is the local radius of curvature (RoC) of the surface in the direction perpendicular to the X–Z plane. In order for the interaction to be adiabatic, we expect that the condition $|\theta_\perp| \ll 1$ must be satisfied in addition to $dZ/dz \approx dZ_m/dz$, since in the limit of an infinitely slow chirp rate, $Y \to 0$ and hence $\theta_\perp \to 0$. Additionally, this angular condition implies a small relative separation of the fields from the local eigenmode, in analogy to conventional adiabatic following processes [40].

With the conditions $|\theta_\perp| \ll 1$ and $dZ/dz = dZ_m/dz$, it is possible to obtain a heuristic constraint on the chirp rate required for the adiabatic following process that in turn can be used to construct apodization profiles. To obtain this constraint, first consider the local curvatures of $\varphi = 0$. Formulas for the curvatures of surfaces specified by implicit equations are given in [41]. We denote the in-plane (X–Z plane) curvature as $k_\parallel$ (RoC $R_\parallel = -k_\parallel^{-1}$), and the curvature in the orthogonal direction as $k_\perp$ (RoC $R_\perp = -k_\perp^{-1}$). After some algebra it can be shown that, at $\mathbf{W}_m$, these curvatures are given by

$$k_\parallel = -\frac{2}{|\nabla\varphi|}\frac{\bar{G}(Z_m) + \nu^2}{1 + \nu^2}, \tag{52a}$$

$$k_\perp = -\frac{2}{|\nabla\varphi|}, \tag{52b}$$

where the parameter $\bar{G}(Z)$ is given by

$$\bar{G}(Z) = 1 + K_{\mathrm{ip}} - 3Z. \tag{53}$$

Given $\mathrm{sgn}(\nu(z_i))$, the relevant local eigenmode and hence $k_\parallel$ and $k_\perp$ are functions of only ν.

An expression for the evolution of the local eigenmode is also required. With Eqs. (48a) and (48c), X_m can be expressed in terms of Z_m. Substituting this result into Eq. (48b), an implicit equation for Z_m is obtained, of the form $f(Z_m(\nu), \nu) = 0$ for function f. By taking the derivative of this $f = 0$ equation with respect to ν, it can be shown that

$$\frac{dZ_m}{d\nu} = -\mathrm{sgn}\left(\frac{d\nu}{dz}\right)\frac{|\nabla\varphi|}{2(\bar{G}(Z_m) + \nu^2)(1 + \nu^2)^{1/2}}, \tag{54}$$

where the sgn prefactor assumes $\nu(\zeta)$ is monotonic. With the above relations and the condition $dZ_m/dz = dZ/dz$, the inequality $|\theta_\perp| \ll 1$ can be expressed as

$$\left|\frac{d}{d(\gamma z)}\left(\frac{\Delta k}{2\gamma g}\right)\right| \ll 2gq(\nu), \tag{55}$$

where the function $q(\nu)$ is defined as

$$q(\nu) = (1 + \nu^2)^{1/2}(\bar{G}(Z_m(\nu)) + \nu^2). \tag{56}$$

Equation (55) is the required adiabaticity condition that we will use to determine AFC apodization profiles. The right hand side is a function only of ν, and hence of Δk_1 and g. It is interesting to note that, if we define a new propagation coordinate $\Xi = \int_{z_i}^{z} \sqrt{(2\gamma g(z'))^2 + \Delta k_1(z')^2}\mathrm{d}z'$, then Eq. (55) can be expressed in an intuitive, purely geometrical form:

$$\left|\frac{d\theta_{\|}}{d\Xi}\right| \ll \frac{k_{\|}}{k_{\perp}}. \tag{57}$$

The form of Ξ arises from Eq. (46): the rate of change of $\mathbf{W}_m$ has an overall scaling with $|\nabla H| = \sqrt{(\gamma g)^2 + (\Delta k/2)^2}$.

We have also found that the fidelity of Eq. (55) is consistent with the values of the output pump depletion predicted by numerical simulations of the CWEs for well-apodized gratings operating in the highly nonlinear, highly saturated regime, as a function of the coupling factor $\lambda_R = \gamma^2/|\Delta k'|$ that we defined in Subsection 6.C. Such consistency helps to support the use of Eq. (55) as an adiabaticity criterion for constructing apodization profiles and for estimating how slow the chirp must be in order for adiabatic following to occur.

Further insight can be gained by considering the region around $|\nu| \approx 1$. In the undepleted-pump limit (in which adiabatic following does not occur), the signal is amplified in the region where $|\nu| < 1$ [1]. Since this limit can be described accurately by the complex WKB method, the points $|\nu| = 1$ are referred to as turning points. For small signal input compared to the pump (small ρ), the turning point closest to the input side of the grating is also an important point in the adiabatic following process: as K_{ip} is increased toward unity ($\rho \to 0$), the ratio $k_{\|}/k_{\perp} \to 0$ near this turning point, and hence, in order to maintain adiabaticity, the chirp rate must be very slow, based on Eq. (57). Physically, the signal must experience a large enough gain to begin depleting the pump over a small region near $|\nu| = 1$ in order to follow the eigenmode. The geometrical explanation for this requirement, provided by Eq. (57), is that the rate at which the eigenmode is swept in the X–Z plane, and hence the required value of Y, scales with $k_{\|}^{-1}$, while the deviation of the angle $\theta_{\perp}$ from zero scales (for a given value of Y) with $k_{\perp}$.

B. AFC Apodization Procedure

We will design apodization profiles such that adiabaticity is maintained, as in previous sections. As before, we also assume that there is a known nominal grating profile to which we append apodization regions. For the reasons discussed in Subsection 4.D, we consider NLCA and not DCA or DDA, and therefore assume $g = 1$. If a range of spectral components are present, then ν and $\mathbf{W}_m$ depend on both frequency and position. Based on Eq. (55) and assuming $g = 1$, we can obtain the following equation for the grating chirp rate within the apodization regions:

$$\left|\frac{dK_g}{dz}\right| = 2\epsilon\gamma^2 \min_{\omega}[q(\nu(z,\omega))], \tag{58}$$

where $\nu(z,\omega) = [\Delta k_0(\omega) - K_g(z)]/(2\gamma(\omega))$ is defined in Eq. (33), $q(\nu)$ is defined in Eq. (56), and minimization is performed over the spectral range of interest. When $q(\nu)$ is small, a slow grating chirp rate is required. We show in Fig. 7 the form of $q(\nu)^{-1}$ for several values of ρ: for small ρ, the minimum of q becomes very small, necessitating a very slow chirp rate.

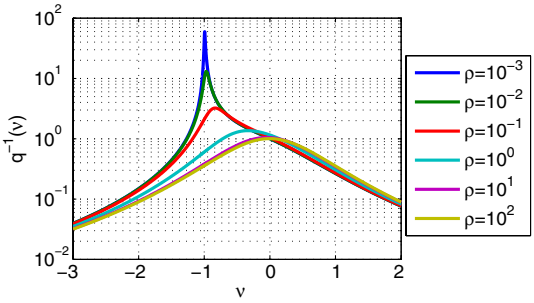

Fig. 7. $q(\nu)^{-1}$ [q defined in Eq. (56), ν defined in Eq. (33)], shown for several values of ρ, assuming a positively chirped grating. For small ρ, the maximum of q^{-1} occurs near the first turning point ($|\nu| = 1$) and diverges as $\rho \to 0$.

Based on Fig. 7 and for a positive QPM chirp rate, the minimum of q is between $\nu = -1$ (obtained for the high-gain OPA limit) and $\nu = 0$ (for the strong-signal, weak-pump DFG limit). Consider positions z for which $\nu(z,\omega)$ is outside of this interval at the edges of the nominal grating profile for all frequencies ω of interest. At these positions, $q(\nu)$ is smallest for the spectral component(s) for which $|\nu|$ is smallest. The apodization regions will begin at points for which this condition holds.

In this section, we will use subscripts – and + to denote the input and output apodization regions, respectively. For a given value of ϵ, we wish to find apodization boundaries $z_{i,\pm}$ for which $\nu(z_{i,\pm},\omega)$ lies outside the interval described above for all ω in the spectral range of interest, and for which Eq. (58) is satisfied for the nominal grating profile. The spectral components for which $|\nu|$ is smallest at these apodization boundaries are denoted $\omega_{\pm}$, and hence satisfy $|\nu(z_{i,\pm},\omega_{\pm})| = \min_{\omega}(|\nu(z_{i,\pm}),\omega)|$. The corresponding values of ν are given by $\nu_{i,\pm} = \nu(z_{i,\pm},\omega_{\pm})$. Thus for $z = z_{i,\pm}$ and $K_g(z) = K_{\mathrm{nom}}(z)$, Eq. (58) is satisfied, and the relevant frequency is $\omega = \omega_{\pm}$.

We now introduce position-dependent but frequency-independent variables derived from ν according to

$$\nu_{\pm}(z) = \frac{\Delta k_0(\omega_{\pm}) - K_g(z)}{2\gamma g(z)}, \tag{59}$$

that satisfy $\nu_{\pm}(z_{i,\pm}) = \nu_{i,\pm}$. $\nu_{\pm}(z)$ are substituted into Eq. (58) to yield a differential equation,

$$\left|\frac{d\nu_{\pm}}{dz}\right| = \epsilon\gamma q(\nu_{\pm}), \tag{60}$$

that can be solved straightforwardly by numerically integrating with respect to $\nu_{\pm}$. Given $\nu_{\pm}(z)$, the grating profile $K_g(z)$ is determined via Eq. (59).

C. AFC Apodization Example

In this subsection, we apply the procedure described in Subsection 7.B to construct an apodization profile for an AFC device. We choose $\rho = 0.2$, corresponding to a case

with a strong pump and moderate-strength signal, in order to illustrate that AFC, and our apodization approach, is effective even when substantial signal gain occurs. We choose a nominally linear grating chirp profile, with $\lambda_R = \gamma^2/|\Delta k'| = 5$, and select $\epsilon = 1/(2\lambda_R)$ so that the apodization regions are 'as adiabatic' as the nominal profile. As in previous sections, we select a nominal grating profile sufficient to support a bandwidth from 1450 to 1650 nm with a 1064 nm pump wavelength, assume a MgO:$LiNbO_3$ device and, in this case, fix $\gamma = \gamma_0 = 3.5 \times 10^3$. The apodization regions are found by solving Eq. (60), as described above, for chosen initial and final values $K_g(z_i)$ and $K_g(z_f)$, respectively.

The simulation is shown in Fig. 8. The pump depletion as a function of signal wavelength is shown in Fig. 8(a) for apodized (NLCA) and unapodized cases. For the apodized case, a very high pump depletion is maintained over the entire target spectrum. In the unapodized case, only a moderate efficiency is predicted, and there are substantial fluctuations in efficiency over the target spectrum. The apodized grating profile is shown in Fig. 8(b), indicating that the apodization regions take up only a relatively small fraction of the device's total length, as in our preceding examples. In practice, achieving high conversion efficiencies will involve a trade-off involving achievable input parameters, amplification of quantum noise, and suppression of unwanted parasitic effects, such as pump SHG [42]. In particular, to achieve a high conversion efficiency at moderate coupling factor λ_R, the ratio of signal and pump photon fluxes at the input the device, ρ, should not be too small. This trade-off between λ_R, ρ, and efficiency was considered in [7].

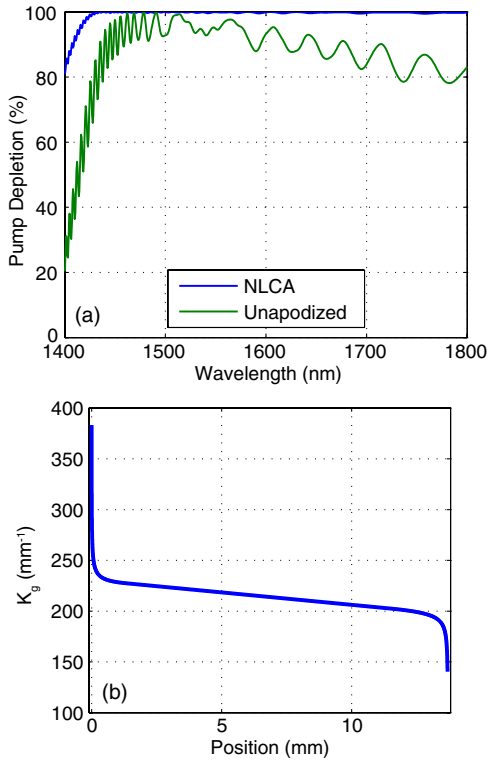

Fig. 8. AFC apodization example, with $\rho = 0.2$ and $\lambda_R = 5$. The remaining parameters are given in the text. (a) Pump depletion versus signal wavelength for apodized and unapodized cases, (b) grating profile $K_g(z)$.

8. DISCUSSION AND CONCLUSIONS

A. Summary

In this paper, we have considered apodization of chirped QPM gratings in detail. Without apodization, such devices exhibit a substantial ripple in spectral amplitude and phase, which is highly disadvantageous to many applications.

We studied most of the main operation regimes of interest. These regimes include the linear regimes of DFG, SFG, SHG, OR, etc., in which only the generated wave is changing substantially; the case of high-gain OPA, in which there is only minor pump depletion; and the case of AFC, in which all of the waves change substantially but remain close to the position-dependent and frequency-dependent nonlinear eigenmode of the TWM process throughout the device. In each of these cases, the structure of the eigenmodes of the unchirped QPM interaction play an important role. We showed, for all of these operating regimes, how apodization profiles can be constructed systematically in order to reach performance limited only by inherent discretization associated with the QPM grating structure. We did not consider SHG with non-negligible pump depletion, but the geometrical analysis of Sections 6 and 7 could be applied to that case as well, and hence we expect adiabatic SHG to occur in properly apodized QPM gratings. We will consider this SHG case and its applications in future work.

We considered different types of apodization, including nonlinear chirp apodization (NLCA), QPM duty cycle apodization (DCA), and deleted-domain apodization (DDA). In principle, comparable performance is achieved by NLCA and DCA. However, DCA is challenging in terms of QPM fabrication since all the domains typically must be created in a single poling event, and the dynamics governing the domain sizes are complicated and difficult to control. Furthermore, DCA typically requires a somewhat larger apodization region. The DDA approach exhibits substantially reduced performance, that we showed for the cases of DFG and OPA. While DDA is well suited to long, unchirped QPM devices, it exhibits poorer performance for chirped QPM devices due to the broad spatial frequency bandwidth of the grating. For the above reasons, we believe that NLCA will usually be the best method of apodizing all types of chirped QPM devices. This conclusion is consistent with our experimental findings [10]. Furthermore, NLCA has the potential to be the least susceptible to photorefractive damage related issues due to its 50% duty cycle [31–33].

In designing apodization profiles, we made sure to maintain the nominal or desired profile of the device for the spectral range of interest. This approach means that nominal grating profiles supporting favorable properties, such as a broad bandwidth or an engineered group delay spectrum, can first be designed [4] and then apodization regions can be appended systematically in order to achieve the desired performance with optimal fidelity. For the case of AFC, this involved constructing a systematic approach to visualizing such devices based on the elegant geometrical description of TWM processes introduced in [28]. Our analysis showed how to both understand and design general AFC devices, even when substantial signal gain and pump depletion are involved simultaneously. The geometrical description also shows clearly why it is difficult to achieve high gain and efficiency simultaneously in AFC devices.

When simulating the QPM designs presented, we used full nonlinear CWEs of the actual discrete QPM grating structures,

without restricting our analysis to the first order QPM approximation. These simulations thus established that the first order QPM approximation is indeed very accurate, even for the more complicated cases of OPA and AFC.

B. QPM Fabrication Considerations

In simulations not shown, we tested the dependence of the devices on the fabrication resolution by "snapping" all of the domain boundaries to a fixed grid of a chosen spacing. We found for the examples presented here (center period ≈30 μm) that even for a grid spacing of up to 1 μm, there is almost no change in device performance. This result means that the typical fabrication grids of 0.1 μm used in lithographic poling are more than sufficient, even for devices with a shorter range of QPM periods. It should be noted, however, that unavoidable random duty cycle (RDC) errors in the QPM grating can enhance the efficiency of unwanted parasitic effects and should not be ignored [42,43].

We emphasize that our procedure for constructing the QPM grating from a designed phase and duty cycle profile, given in Eq. (3), in general makes the device insensitive to the discrete nature of the QPM domains, since it ensures that the higher spatial frequencies of the grating are always separated by an integer number of "carrier frequencies" of the grating, and therefore have minimal overlap with the first Fourier order.

For fabricating apodized gratings, it is important to note that there is typically some uncertainty in the actual crystal length due to variations in the amount of material lost during polishing. Unless care is taken, these fluctuations could end up removing the most highly phase mismatched parts of the device, since the grating period is increased very rapidly over a short distance at the edges of the grating. One way to resolve this issue is by having an unpoled gap between the ends of the crystal and the ends of the designed grating. However, such unpoled regions will introduce an additional spectral ripple and can be very disadvantageous in the context of photorefractive effects, as mentioned above [31–33]. Instead, one could make simple modifications to the apodization procedures presented here to ensure a slow chirp rate at the edges of the grating (i.e., the chirp rate is first increased rapidly, then decreased again near the edges of the grating, while still satisfying the required inequalities and maintaining a monotonic $K_g(z)$ profile). In this way, the range of spatial frequencies present on the device can be made insensitive to the polishing process.

If there is a single poling event, and if it can be assumed that the domains are independent of each other and their position on the wafer, then the local duty cycle will be determined by the local period. This period dependence of the duty cycle could, in principle, be accounted for in the design, at least to the extent that it is known. One could express the duty cycle D as a function of grating k-vector K_g, and substitute the resulting form $g(K_g(z))$ into the inequalities we discussed. Since these subtleties are determined mainly by QPM fabrication issues rather than QPM device physics, we did not discuss them in detail here, but they could be accounted for with minor extensions of the methods presented.

C. Spatiotemporal Apodization

In this paper, we have not considered solitons and solitary waves either in the spatial or temporal domain [44]. AFC offers the potential for high conversion efficiency across a nonuniform spatial and temporal profile, but parasitic processes associated with overdriving the center of the beams present a potential limitation of this approach. Therefore, some applications could benefit significantly from approaches, such as adiabatic soliton evolution [45]. Since many of our results draw on concepts of local eigenmodes, they are likely to apply to such interactions as well, but analysis of these cases is beyond the scope of this paper. Instead, based on practical considerations, we have used plane wave models in order to obtain results that are not reliant on or strongly constrained by diffractive effects. Nonetheless, care should be taken in order to avoid excessive excitation of three-wave modulation instabilities that can be associated with three-wave nonlinear eigenmodes [44]; these and other spatial effects relevant to the design of highly nonlinear chirped QPM devices will be the subject of future work.

An alternative way of viewing such spatiotemporal effects is as a means of QPM apodization. That is, to have beams or pulses that are initially nonoverlapping in space or time, respectively, and fully walk across each other's spatial or temporal profiles as they propagate through the nonlinear crystal. In this way, components generated by mixing between these two beams/pulses will be apodized, since the interaction is smoothly turned on and off via walk-off. In principle, one could also use beams that diffract strongly within the crystal so that the intensities are low at the input and output ends and increase slowly toward the focus.

A drawback of such schemes is that they could strongly influence the desired interaction, or change it entirely. We have found, for example, that excessive group velocity walk-off can lead to additional spectral ripples in nonlinear chirped QPM interactions, such as AFC. Furthermore, walk-off based schemes will necessitate significantly longer crystals at a given optical intensity, and hence will exacerbate any unwanted parasitic effects that scale with the device length. Therefore, while spatiotemporal apodization schemes may find use in some contexts, we have not considered them in detail here.

One case that is of interest and can be suitably engineered is waveguide-coupling-based apodization, as discussed in [24]. Having the two input waves initially in different waveguides and then adiabatically coupled to each other is analogous, in this context, to a smooth modulation of $g(z)$ from ≈0 to ≈1, and therefore may be of continued interest for waveguide-based apodization, particularly since DDA, the preferred approach from [24] for apodizing periodic gratings, is less suited to chirped QPM devices. For example, one could imagine combining a NLCA scheme with a waveguide-coupling-based amplitude apodization to further suppress spectral ripples beyond the limits imposed here by the discrete nature of the QPM grating.

D. Conclusions

The difficulty in fabricating duty-cycle-modulated QPM gratings, combined with the high versatility of chirped QPM gratings, means that such devices will continue to play a central role in QPM technology. In addition to efficient frequency conversion, our apodization techniques could be applied to efficiently excite nonlinear eigenmodes at a chosen finite phase mismatch; for example, in the context of cascaded $\chi^{(2)}$

interactions. The systematic study of device operation and apodization we have presented here should therefore be of critical importance to the continued development of QPM technology and its applications.

ACKNOWLEDGMENT

This research was supported by the U.S. Air Force Office of Scientific Research (AFOSR) under grants FA9550-05-1-0180 and FA9550-09-1-0233.

REFERENCES

1. M. Charbonneau-Lefort, B. Afeyan, and M. M. Fejer, "Optical parametric amplifiers using chirped quasi-phase-matching gratings I: practical design formulas," J. Opt. Soc. Am. B **25**, 463–480 (2008).
2. G. Imeshev, M. M. Fejer, A. Galvanauskas, and D. Harter, "Pulse shaping by difference-frequency mixing with quasi-phase-matching gratings," J. Opt. Soc. Am. B **18**, 534–539 (2001).
3. G. Imeshev, M. A. Arbore, M. M. Fejer, A. Galvanauskas, M. Fermann, and D. Harter, "Ultrashort-pulse second-harmonic generation with longitudinally nonuniform quasi-phase-matching gratings: pulse compression and shaping," J. Opt. Soc. Am. B **17**, 304–318 (2000).
4. M. Charbonneau-Lefort, M. M. Fejer, and B. Afeyan, "Tandem chirped quasi-phase-matching grating optical parametric amplifier design for simultaneous group delay and gain control," Opt. Lett. **30**, 634–636 (2005).
5. M. Charbonneau-Lefort, B. Afeyan, and M. M. Fejer, "Competing collinear and noncollinear interactions in chirped quasi-phase-matched optical parametric amplifiers," J. Opt. Soc. Am. B **25**, 1402–1413 (2008).
6. L. Gallmann, G. Steinmeyer, U. Keller, G. Imeshev, M. M. Fejer, and J. Meyn, "Generation of sub-6 fs blue pulses by frequency doubling with quasi-phase-matching gratings," Opt. Lett. **26**, 614–616 (2001).
7. C. R. Phillips and M. M. Fejer, "Efficiency and phase of optical parametric amplification in chirped quasi-phase-matched gratings," Opt. Lett. **35**, 3093–3095 (2010).
8. H. Suchowski, V. Prabhudesai, D. Oron, A. Arie, and Y. Silberberg, "Robust adiabatic sum frequency conversion," Opt. Express **17**, 12731–12740 (2009).
9. C. Heese, C. R. Phillips, B. W. Mayer, L. Gallmann, M. M. Fejer, and U. Keller, "75 MW few-cycle mid-infrared pulses from a collinear apodized APPLN-based OPCPA," Opt. Express **20**, 26888–26894 (2012).
10. C. Heese, C. R. Phillips, L. Gallmann, M. M. Fejer, and U. Keller, "Role of apodization in optical parametric amplifiers based on aperiodic quasi-phasematching gratings," Opt. Express **20**, 18066–18071 (2012).
11. C. Heese, C. R. Phillips, L. Gallmann, M. M. Fejer, and U. Keller, "Ultrabroadband, highly flexible amplifier for ultrashort midinfrared laser pulses based on aperiodically poled Mg:$LiNbO_3$," Opt. Lett. **35**, 2340–2342 (2010).
12. C. R. Phillips, L. Gallmann, and M. M. Fejer, "Design of quasi-phasematching gratings via convex optimization," Opt. Express **21**, 10139–10159 (2013).
13. C. Langrock, M. M. Fejer, I. Hartl, and M. E. Fermann, "Generation of octave-spanning spectra inside reverse-proton-exchanged periodically poled lithium niobate waveguides," Opt. Lett. **32**, 2478–2480 (2007).
14. C. R. Phillips, C. Langrock, J. S. Pelc, M. M. Fejer, I. Hartl, and M. E. Fermann, "Supercontinuum generation in quasi-phase-matched waveguides," Opt. Express **19**, 18754–18773 (2011).
15. C. R. Phillips, C. Langrock, J. S. Pelc, M. M. Fejer, J. Jiang, M. E. Fermann, and I. Hartl, "Supercontinuum generation in quasi-phase-matched $LiNbO_3$ waveguide pumped by a Tm-doped fiber laser system," Opt. Lett. **36**, 3912–3914 (2011).
16. M. Conforti, F. Baronio, and C. De Angelis, "Nonlinear envelope equation for broadband optical pulses in quadratic media," Phys. Rev. A **81**, 053841 (2010).
17. K. A. Tillman, D. T. Reid, D. Artigas, J. Hellström, V. Pasiskevicius, and F. Laurell, "Low-threshold femtosecond optical parametric oscillator based on chirped-pulse frequency conversion," Opt. Lett. **28**, 543–545 (2003).
18. K. A. Tillman and D. T. Reid, "Monolithic optical parametric oscillator using chirped quasi-phase matching," Opt. Lett. **32**, 1548–1550 (2007).
19. C. R. Phillips and M. M. Fejer, "Adiabatic optical parametric oscillators: steady-state and dynamical behavior," Opt. Express **20**, 2466–2482 (2012).
20. C. R. Phillips and M. M. Fejer, "Stability of the singly resonant optical parametric oscillator," J. Opt. Soc. Am. B **27**, 2687–2699 (2010).
21. T. W. Neely, L. Nugent-Glandorf, F. Adler, and S. A. Diddams, "Broadband mid-infrared frequency upconversion and spectroscopy with an aperiodically poled $LiNbO_3$ waveguide," Opt. Lett. **37**, 4332–4334 (2012).
22. Y. Deng, A. Schwarz, H. Fattahi, M. Ueffing, X. Gu, M. Ossiander, T. Metzger, V. Pervak, H. Ishizuki, T. Taira, T. Kobayashi, G. Marcus, F. Krausz, R. Kienberger, and N. Karpowicz, "Carrier-envelope-phase-stable, 1.2 mJ, 1.5 cycle laserpulses at 2.1 μm," Opt. Lett. **37**, 4973–4975 (2012).
23. V. J. Hernandez, C. V. Bennett, B. D. Moran, A. D. Drobshoff, D. Chang, C. Langrock, M. M. Fejer, and M. Ibsen, "104 MHz rate single-shot recording with subpicosecond resolution using temporal imaging," Opt. Express **21**, 196–203 (2013).
24. J. Huang, X. P. Xie, C. Langrock, R. V. Roussev, D. S. Hum, and M. M. Fejer, "Amplitude modulation and apodization of quasi-phase-matched interactions," Opt. Lett. **31**, 604–606 (2006).
25. T. Umeki, M. Asobe, Y. Nishida, O. Tadanaga, K. Magari, T. Yanagawa, and H. Suzuki, "Widely tunable 3.4 μm band difference frequency generation using apodized $\chi^{(2)}$ grating," Opt. Lett. **32**, 1129–1131 (2007).
26. A. Tehranchi and R. Kashyap, "Design of novel unapodized and apodized step-chirped quasi-phase matched gratings for broadband frequency converters based on second-harmonic generation," J. Lightwave Technol. **26**, 343–349 (2008).
27. A. Bostani, A. Tehranchi, and R. Kashyap, "Engineering of effective second-order nonlinearity in uniform and chirped gratings," J. Opt. Soc. Am. B **29**, 2929–2934 (2012).
28. G. G. Luther, M. S. Alber, J. E. Marsden, and J. M. Robbins, "Geometric analysis of optical frequency conversion and its control in quadratic nonlinear media," J. Opt. Soc. Am. B **17**, 932–941 (2000).
29. R. W. Boyd, *Nonlinear Optics*, 3rd ed. (Academic, 2008).
30. G. D. Miller, "Periodically poled lithium niobate: modeling, fabrication, and nonlinear-optical performance," Ph.D. dissertation (Stanford University, 1998).
31. M. Taya, M. C. Bashaw, and M. M. Fejer, "Photorefractive effects in periodically poled ferroelectrics," Opt. Lett. **21**, 857–859 (1996).
32. J. R. Schwesyg, M. Falk, C. R. Phillips, D. H. Jundt, K. Buse, and M. M. Fejer, "Pyroelectrically induced photorefractive damage in magnesium-doped lithium niobate crystals," J. Opt. Soc. Am. B **28**, 1973–1987 (2011).
33. C. R. Phillips, J. S. Pelc, and M. M. Fejer, "Continuous wave monolithic quasi-phase-matched optical parametric oscillator in periodically poled lithium niobate," Opt. Lett. **36**, 2973–2975 (2011).
34. C. M. Bender and S. A. Orszag, *Advanced Mathematical Methods for Scientists and Engineers I: Asymptotic Methods and Perturbation Theory*, Vol. **1** (Springer, 1999).
35. G. I. Stegeman, D. J. Hagan, and L. Torner, "$\chi^{(2)}$ cascading phenomena and their applications to all-optical signal processing, mode-locking, pulse compression and solitons," Opt. Quantum Electron. **28**, 1691–1740 (1996).
36. H. Steigerwald, F. Luedtke, and K. Buse, "Ultraviolet light assisted periodic poling of near-stoichiometric, magnesium-doped lithium niobate crystals," Appl. Phys. Lett. **94**, 032906 (2009).
37. C. Conti, S. Trillo, P. Di Trapani, J. Kilius, A. Bramati, S. Minardi, W. Chinaglia, and G. Valiulis, "Effective lensing effects in parametric frequency conversion," J. Opt. Soc. Am. B **19**, 852–857 (2002).
38. R. B. White, *Asymptotic Analysis of Differential Equations* (World Scientific, 2005).

39. J. A. Armstrong, N. Bloembergen, J. Ducuing, and P. S. Pershan, "Interactions between light waves in a nonlinear dielectric," Phys. Rev. **127**, 1918–1939 (1962).
40. M. D. Crisp, "Adiabatic-Following approximation," Phys. Rev. A **8**, 2128–2135 (1973).
41. R. Goldman, "Curvature formulas for implicit curves and surfaces," Comput. Aided Geom. Des. **22**, 632–658 (2005).
42. C. R. Phillips, J. S. Pelc, and M. M. Fejer, "Parametric processes in quasi-phasematching gratings with random duty cycle errors," J. Opt. Soc. Am. B **30**, 982–993 (2013).
43. J. S. Pelc, C. R. Phillips, D. Chang, C. Langrock, and M. M. Fejer, "Efficiency pedestal in quasi-phase-matching devices with random duty-cycle errors," Opt. Lett. **36**, 864–866 (2011).
44. A. V. Buryak, P. D. Trapani, D. V. Skryabin, and S. Trillo, "Optical solitons due to quadratic nonlinearities: from basic physics to futuristic applications," Phys. Rep. **370**, 63–235 (2002).
45. S. Ashihara, J. Nishina, T. Shimura, and K. Kuroda, "Soliton compression of femtosecond pulses in quadratic media," J. Opt. Soc. Am. B **19**, 2505–2510 (2002).